Monthly Notices of the ROYAL ASTRONOMICAL SOCIETY

MNRAS **545,** 1–22 (2026) https://doi.org/10.1093/mnras/staf2036
Advance Access publication 2025 November 19

Planetary nebulae as tracers of stellar population properties: a pilot study with MUSE

Ana Inés Ennis,[1,2]★ Johanna Hartke,[3,4,5] Fuyan Bian,[6,7] Claudia Pulsoni,[8] Chiara Spiniello,[9,10] Magda Arnaboldi[11] and Roberto de Propris[3,4,12]

[1]*Perimeter Institute for Theoretical Physics, Waterloo, 31 Caroline St. North, Canada*
[2]*Waterloo Centre for Astrophysics, University of Waterloo, Physics Department, Waterloo, ON N2L 3G1, Canada*
[3]*Finnish Centre for Astronomy with ESO (FINCA),University of Turku, FI-20014 Turku, Finland*
[4]*Department of Physics and Astronomy, Tuorla Observatory,University of Turku, FI-20014 Turku, Finland*
[5]*Turku Collegium for Science, Technology and Medicine (TCSMT),University of Turku, FI-20014 Turku, Finland*
[6]*European Southern Observatory, Alonso de Córdova, Vitacura, Santiago, Chile*
[7]*Chinese Academy of Sciences South America Center for Astronomy, National Astronomical Observatories, CAS, Beijing 100101, China*
[8]*Max-Planck-Institut für Extraterrestrische Physik (MPE), Gießenbachstraße 1, D-85748 Garching bei München, Germany*
[9]*Department of Physics, University of Oxford, Denys Wilkinson Building, Keble Road, Oxford OX1 3RH, UK*
[10]*INAF – Osservatorio Astronomico di Capodimonte, Salita Moiariello 16, I-80131 Napoli, Italy*
[11]*European Southern Observatory, Karl-Schwarzschild-Straße 2, D-85748 Garching bei München, Germany*
[12]*Department of Physics and Astronomy, Botswana International University of Science and Technology, Plot 10071, Private Bag 16, Palapye, Botswana*

Accepted 2025 November 13. Received 2025 November 7; in original form 2025 August 22

ABSTRACT

Planetary nebulae (PNe) are the only single stars in galaxies outside the Local Group that can be used as kinematic tracers of the diffuse light in the extended halo. Analysing their luminosity-specific number density across galaxies of different morphologies has also shown hints that they may be used as tracers of the age and metallicity of stellar populations. A proper understanding of this relation has been hindered by the fact that simultaneously detecting PNe and accurately measuring stellar properties is extremely difficult using classical narrow-band imaging methods, which cannot detect PNe in the bright centres of galaxies. In this work, we use integral-field spectroscopy to overcome this challenge, analysing the inner regions of a sample of 10 early-type galaxies from the Extended Planetary Nebulae Survey (ePN.S) for which archival MUSE data were available. With the Diffuse Emission-Line Filter (DELF) technique, we automate the detection of PNe, and perform spectral fitting on the diffuse light to infer kinematics and stellar population parameters. We compare the PN number density profile and its associated α-parameter with multiple properties of the host galaxies. We find that our sample follows the previously observationally constrained correlation with the metallicity of the host galaxy. We find a weak anticorrelation between the α-parameter and the far-ultraviolet excess, highlighting the possible relation between the visibility lifetime of PNe on the spectral energy distribution of their host galaxies, with fewer PNe detected in association with stellar populations characterized by an ultraviolet excess.

Key words: planetary nebulae: general – galaxies: elliptical and lenticular, cD – galaxies: evolution – galaxies: kinematics and dynamics – galaxies: stellar content.

1 INTRODUCTION

Towards the end of their lives, stars with initial masses between ~ 1 and $8\,M_\odot$ go through the planetary nebula (PN) phase, instead of exploding as supernovae. During this stage, the central star is surrounded by an envelope of material where recombination and photoionization are happening simultaneously. This creates the distinct optical spectral features of a PN: a flat continuum with prominent emission lines, with one of the strongest emissions being at the 5007 Å forbidden [O III] line. This line is intense enough to be singularly detected from individual PNe at large distances (~ 100 Mpc; O. Gerhard et al. 2005). This has led PNe to become one of the most widely used kinematic tracers for the stellar populations in galaxy haloes (e.g. L. Coccato et al. 2009; C. Pulsoni et al. 2018, 2023; J. Hartke et al. 2022; S. Bhattacharya et al. 2023), serving as tools to unveil tidal substructures and to further our understanding of dark matter haloes. PNe are also viable kinematic tracers of the diffuse intracluster light (e.g. M. Arnaboldi et al. 1996; O. Gerhard et al. 2005; A. Longobardi et al. 2015; J. Hartke et al. 2018; M. Arnaboldi & O. Gerhard 2022).

PN populations in nearby early- and late-type galaxies (LTGs) have been shown to follow a near-universal luminosity function (R. Ciardullo et al. 2002, 2004), generally well described within 2.5 magnitudes by

$$N(M_{5007}) = c_1 e^{c_2 M_{5007}} \left(1 - e^{3(M^* - M_{5007})}\right), \quad (1)$$

★ E-mail: ennis.ana@gmail.com

© The Author(s) 2025.
Published by Oxford University Press on behalf of Royal Astronomical Society. This is an Open Access article distributed under the terms of the Creative Commons Attribution License (https://creativecommons.org/licenses/by/4.0/), which permits unrestricted reuse, distribution, and reproduction in any medium, provided the original work is properly cited.

where M_{5007} is the absolute magnitude of the 5007 Å line, c_1 is a normalization constant, and M^* is the absolute magnitude of the bright cut-off, which has empirically been shown to be nearly constant at $M^* = -4.51^{+0.02}_{0.04}$ (R. Ciardullo et al. 2002, 2004). The shape of the analytic PNLF is motivated by the physics of PNe, with the first term describing how the surface brightness of the envelope around the central star is fading as it expands with constant velocity (K. G. Henize & B. E. Westerlund 1963). The slope $c_2 = 0.307$, considered constant in the original implementation of the function, has since been found to vary. A. Longobardi et al. (2013) were the first to introduce a PNLF with variable faint-end slope, which is thought to be connected to the properties of the underlying stellar populations. Steeper PNLFs have been associated with older metal-poor stellar populations, while flatter slopes may be connected to younger stars (R. Ciardullo et al. 2004; R. Ciardullo 2010; A. Longobardi et al. 2013; J. Hartke et al. 2020). In some star-forming galaxies, the PNLF has been shown to deviate from this equation for faint PNe, presenting dips (G. H. Jacoby & O. De Marco 2002; L. Hernández-Martínez & M. Peña 2009). Due to the universality of the bright cut-off, the PNLF is used to estimate extragalactic distances (R. Ciardullo et al. 1989; A. Buzzoni, M. Arnaboldi & R. L. M. Corradi 2006; G. H. Jacoby et al. 2024). Recently, L. M. Valenzuela et al. (2025) have started to analyse PNe within cosmological simulations, looking to uncover the physical pathway for the PNLF, its shape, and its cut-off.

The luminosity-specific PN number density, commonly known as the α-parameter, estimates the size of the PN population in a galaxy in relation to its luminosity (G. H. Jacoby 1989),

$$N_{\rm PN} = \alpha L_{\rm bol}. \tag{2}$$

Depending on the depth/sensitivity of the survey, $\alpha_{\Delta m}$ refers to the limit in fainter magnitudes below the bright cut-off magnitude of the PNLF reached by the survey. The total number of PNe, $N_{\rm PN}$, for a chemically uniform single-age stellar population can be described in terms of the specific evolutionary flux, $\mathcal{B}$, and the PN visibility lifetime, $\tau_{\rm PN}$:

$$N_{\rm PN} = \mathcal{B}\, L_{\rm bol}\, \tau_{\rm PN} \tag{3}$$

In the simple stellar populations (SSP) framework (A. Renzini & A. Buzzoni 1986; A. Buzzoni 1989), $\mathcal{B}$ is defined as the rate of stars leaving the main sequence normalized by the unit light. The $\tau_{\rm PN}$ refers to the PN visibility lifetime, which is not the same as the time spent in the PN evolutionary phase. In particular, $\tau_{\rm PN}$ depends heavily in the properties of the ejected material and the core-mass evolution of the central star. Therefore, the α-parameter links the important PN phase parameters with some of the average properties of their parent stellar component.

Observationally, the α-parameter has been found to correlate with the colour and morphology of the galaxy, as described initially in A. Buzzoni et al. (2006), B06 from here on. This seminal work thoroughly investigated the α-parameter-galaxy connection through the use of population synthesis models, comparing theoretical results with a diverse observational sample. They calculate the α-parameter based on the SSP theory derived by A. Renzini & A. Buzzoni (1986) and A. Buzzoni (1989), taking into consideration the chemical and dynamical properties of PN and stellar evolution tracks, and applying them to template galaxy models. The main theoretical prediction from this analysis is that the α-parameter should moderately increase from star-forming/blue galaxies to quiescent/red ones, with the former hosting smaller PNe populations and a having lower mass/luminosity ratios. Observationally, the earliest work to investigate the empirical correlations is R. Ciardullo, G. H. Jacoby & W. E. Harris (1991), where for a sample of 10 galaxies the α-parameter is shown to be strongly correlated with the U-V index, showing the opposite trend than the one predicted by theory, with blue galaxies producing more PNe. Studies over the following decade have continued to corroborate this result, contrary to the theoretical models, with improved techniques and more accurate measurements, in particular R. Ciardullo et al. (2005) where the analysed correlations include optical colour of the host galaxy, the ultraviolet (UV) upturn, and the Hβ absorption line, used as an indicator of the age of the population.

In recent works, the α-parameter has been shown to vary across different regions of a single galaxy, which may be linked to changes in the age and metallicity of the stellar populations (A. Longobardi et al. 2013; J. Hartke et al. 2017, 2020; S. Bhattacharya et al. 2019). This dependence is promising since it could turn PNe into tracers of stellar population properties of stellar haloes, and, in the cases of cluster galaxies, the surrounding intracluster light. These α-parameter variations have implications for our understanding of stellar evolution, since the α-parameter is related to the visibility lifetime ($\tau_{\rm PN}$) of PN, which depends on properties of the central stars and their ejected material (A. Renzini & A. Buzzoni 1986; A. Buzzoni 1989; A. Buzzoni et al. 2006; F. Annibali et al. 2017).

The main challenge in understanding the possible relation between stellar age and metallicity and the α-parameter lies in the fact that PNe are commonly studied in regions where the properties of stellar populations cannot be easily measured. The central regions of galaxies, where direct measurements of stellar population properties are easily obtained, are thought to have distinct formation pathways from the extended halo, where PNe are traditionally observed. Physical properties thus vary with radius across galaxies, in particular age and metallicity (L. Coccato, O. Gerhard & M. Arnaboldi 2010; N. Pastorello et al. 2014; S. Zibetti et al. 2020; C. M. Cheng et al. 2024). This means that simultaneously analysing the stellar component and the α-parameter of PNe in the same regions of galaxies for a significant sample of galaxies is a key step in unlocking the physical reasons behind the apparent correlation.

Classical detection methods such as the on-off technique, which is based on narrow-band imaging covering the [O III] emission (on) in comparison with broad-band imaging away from the [O III] emission (off), suffer from blind spots in the central regions of galaxies, where the galaxy outshines the PNe.[1] In the last decade, integral field spectroscopy (IFS) has emerged as a tool to untangle emission in these regions, both with instruments on 4-m telescopes (e.g. M. Sarzi et al. 2011), and with MUSE on the 8.2-m VLT (e.g. K. Kreckel et al. 2017; M. M. Roth et al. 2018). Based on the classical on-off technique, M. M. Roth et al. (2021) developed a method called 'Diffuse Emission-Line Filter (DELF)', which facilitates the detection of emission-line sources in high surface brightness regions of galaxies on to which we build in this paper.

In this work we aim to detect PNe in the inner regions of early-type galaxies (ETGs) in order to connect their properties with that of PNe located further from the centre. We use archival data of 10 ETGs located in dense environments to detect and characterize PNe, and, at the same time, obtain the properties of the parent stellar population, such as age and metallicity. By exploring the potential of MUSE data in the ESO Science Archive, we correlate the PN samples with the accurate and spatially resolved measurements of

[1] In classical narrow-band imaging, the Possionian noise of the continuum in a few tens Å band pass is of the same order of the flux from the brightest PN

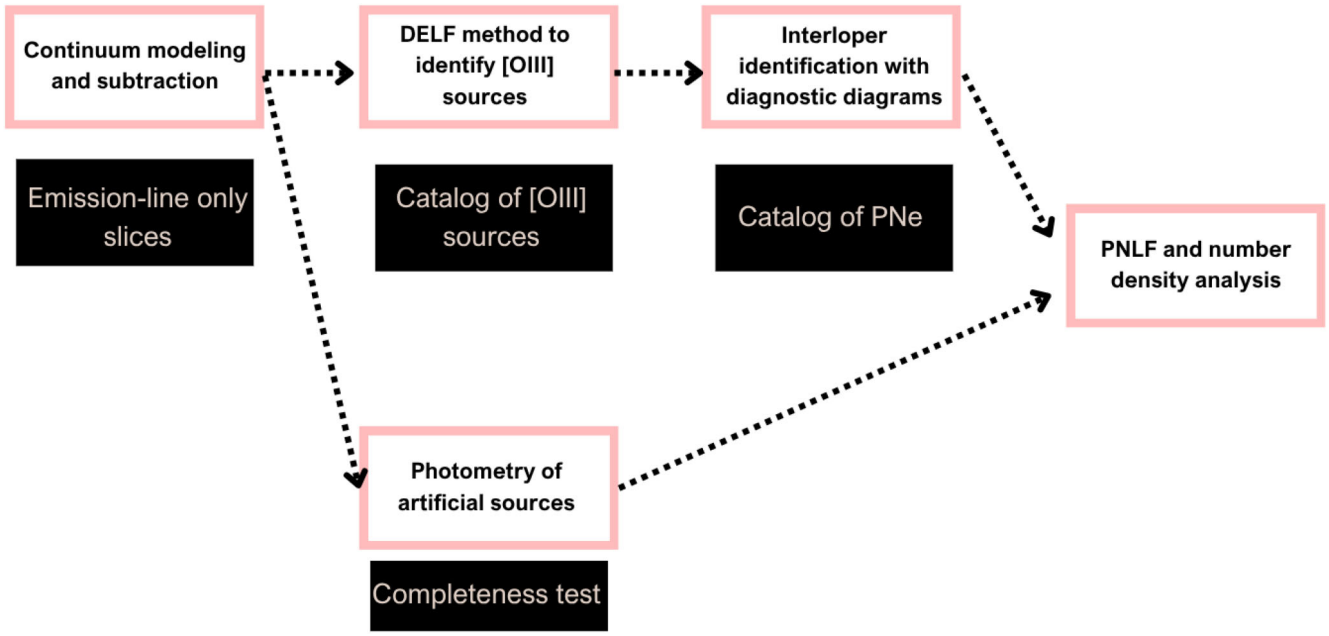

Figure 1. Flowchart describing the method used to perform the analysis carried out in this paper.

the stellar population properties in the bright centres of ETGs that are allowed by the IFS (H. Kuntschner et al. 2010; R. M. McDermid et al. 2015). The goals are to allow us to correlate the α-parameter and other parameters all measured in the same spatial regions.

This paper is organized as follows. In Section 2 we present the sample of archival MUSE observations. In Section 3 we derive spatially resolved stellar kinematics and population properties. In Sections 4 and 5 we present our automatized PN detection method and subsequent analysis of the PN samples, shown in Fig. 1 for reference. Finally, in Section 6, we discuss our results and contrast PN and stellar population properties. We conclude the paper in Section 7. Throughout the paper, we adopt distances based on surface brightness fluctuations (SBFs) from R. B. Tully et al. (2013) (compilation based on the sample from J. L. Tonry et al. 2001 with modifications by J. P. Blakeslee et al. 2010) for the selected galaxies. There is a zero-point systematic of about 0.2 mag between PNLF and SBF distances, which will affect our bright cut-off measurements but since it is homogeneously applied throughout the sample it does not impact the analysis.

2 DATA REDUCTION AND SAMPLE SELECTION

2.1 Observations and data reduction

The observations were obtained from the Science Portal in the ESO Archive, where processed data are readily available from the MUSE science data collection (https://doi.eso.org/10.18727/archive/41). All data cubes used in this work were observed using the MUSE spectrograph (R. Bacon et al. 2010), located at the Nasmyth B focus of Yepun, the 8.2 m VLT UT4 telescope. The observations in every case were made in wide-field mode, covering a 1×1 field of view (FoV) with a pixel scale of 0.2 arcsec. The spectral coverage of MUSE is $\sim$ 4800–9300 Å, with a spectral sampling of 1.25 Å, and a spectral resolution of $\sim$ 2.6 Å. The data products were obtained from the ESO Archive Science Portal, and they were produced by ESO with the standard pipeline (P. M. Weilbacher et al. 2020). The exception were the commissioning data for NGC 3115, which we reduced ourselves with the standard MUSE data reduction pipeline and the dedicated calibrations for this commissioning run since only raw data were available.

2.2 Sample selection

We built our sample of galaxies, listed in Table 1, based on the extended Planetary Nebula Spectrograph (ePN.S) ETG survey (C. Pulsoni et al. 2018) and the Fornax Cluster VLT Spectroscopic Survey (C. Spiniello et al. 2018), selecting those for which MUSE science data were available in the ESO archive,[2] with the goal of analysing the α-parameter properties across entire galaxies as future work. We discarded those with cubes that lacked the required depth due to limited exposure times. The sample contains galaxies located up to a distance of 25 Mpc, a constraint inherited from the ePN.S sample. Due to the range of distances, the variety of pointings and the presence of dust or emission sources, we cover different galactocentric distances in each galaxy.

All galaxies in our sample are massive ($10 < \log \mathrm{M_{gal}}/\mathrm{M_\odot} < 11.5$) ETGs, meaning their stellar populations are old, and mainly metal-rich, which constrains the range of analysed properties in comparison with B06, which includes LTGs. In the following text we will use the galaxy NGC 1387 as a test case, describing the analysis that is performed on all the ETGs in the sample. The results for the rest of the sample is shown in Appendix A and Appendix B.

3 STELLAR POPULATION ANALYSIS

3.1 Stellar kinematics

We utilized the Galaxy IFU Spectroscopy Tool (GIST; A. Bittner et al. 2019) to calculate the properties of the stellar component from absorption spectroscopy. This pipeline provides a framework for

[2] https://archive.eso.org/scienceportal/home

Table 1. Galaxies included in the sample. The asterisks indicate galaxies for which observations with different exposure times were considered. All distances are from R. B. Tully et al. (2013), where measurements are compiled from J. L. Tonry et al. (2001), with small modifications from J. P. Blakeslee et al. (2010). Other observations for NGC 3115 currently available in the archive were not used due to the seeing conditions being inadequate for this work. Morphologies are from [1]: S. S. Kartha et al. (2014) and [2]: G. Vaucouleurs et al. (1991).

Galaxy	Distance (Mpc)	Redshift	Morph. type	m_B	Total exposure time (s)	Seeing (arcsec)	ESO programme ID
NGC 1387	19.1	0.0043	S0[1]	11.75	3600	0.82	296.B-5054
NGC 1399	22.1	0.0047	E1[2]	9.74	7155	0.89	094.B-028 & 094.B-0903
NGC 1404	19.5	0.0065	E1[2]	10.69	3600	0.83/0.89	296.B-5054
NGC 3115	9.5	0.0023	S0	11	600	0.	60.A-9100(A)
NGC 3379	10.2	0.001825	E1[2]	10.56	1656	0.	108.21ZY
NGC 4365	22.8	0.0041	E3[2]	11.5	2502	1.03	094.B-0225
NGC 4374	16.9	0.0034	E1[2]	12.09	1200	0.68	0102.B-0048
NGC 4472	16.1	0.0033	E2[2]	13.21	1800	0.88	095.B-0295
NGC 4594	11.3	0.0034	E2[2]	9.55	2700–3600∗	1.03–1.43	60.A-9303
NGC 5128	3.6	0.0018	S0 pec[2]	8.18	−∗	1.2–1.7	094.B-0298

the use of spectral analysis tools on data cubes, with a default set-up specific to MUSE. As a first step, we masked background objects and foreground stars. Then, we used a signal-to-noise ratio (SNR) target value of 150 to spatially bin the pixels using the Voronoi tessellation routine (M. Cappellari & Y. Copin 2003). Despite MUSE providing us a larger spectral range, for this part of the analysis, we restricted the spectra to 4750–6000 Å, since beyond 6000 Å strong emission and sky lines contaminate both the SNR estimation required for the binning and the measurement of any properties. We also manually masked sky lines and strong emission lines.

Through GIST, we ran pPXF (M. Cappellari & E. Emsellem 2004; M. Cappellari 2017) to measure the kinematics of the underlying stellar population. We used templates from the MILES spectral library (A. Vazdekis et al. 2010), covering ages between 0.03 and 14 Gyr, and metallicities in the range $-2.27 < [M/H] < +0.40$. The SSP models used to generate these libraries are based on BaSTI isochrones (A. Pietrinferni et al. 2004, 2006, 2009, 2013) and the revised Kroupa initial mass function (P. Kroupa 2001).[3] We used 25 additive Legendre polynomial, and extracted four kinematic moments, corresponding to the coefficients in the velocity profile expansion to a Gauss–Hermite series (R. P. der Marel & M. Franx 1993; O. E. Gerhard 1993).

3.2 Stellar population properties

In Fig. 2 we show the line-of-sight (LOS) velocity V, the dispersion, σ, and the parameters h_3 and h_4, for NGC 1387.[4]

The results are consistent with those by E. Iodice et al. (2019), where the same data are also analysed with pPXF, but outside of the GIST framework. The bar in the centre of NGC 1387 defines the structure we see in the kinematics, generating the high σ values ($\sigma > 200\,\mathrm{km\,s^{-1}}$) in the central region and probably influencing the annular structure seen in the σ distribution as well. h_3 and h_4 are close to 0 as expected, though in the central region, the latter goes to higher values, which is consistent with the presence of the bar, disc, and bulge in this area.

We then determined the age and metallicity distribution of the stellar population of the galaxies in the sample by using pPXF in GIST to calculate a non-parametric star formation history, using 25 multiplicative Legendre polynomials and a regularization error of 1 (M. Cappellari 2017). In Fig. 3 we show the results for NGC 1387, for which we measure old ages, consistent with an ETG, and a steep metallicity gradient, going from supersolar to sub-solar, at increasing galactocentric distances. In the region where the bar is situated, we find younger more metal-rich stars, indicating a connection between the structure and a starburst episode.

For the rest of the sample, we compared with ATLAS3D (M. Cappellari et al. 2011), Fornax3D (I. Martín-Navarro et al. 2021), and A. Guérou et al. (2016), to ensure overall compatibility between our results and those previously available. Some slight differences were found, however, average properties were found to be consistent.

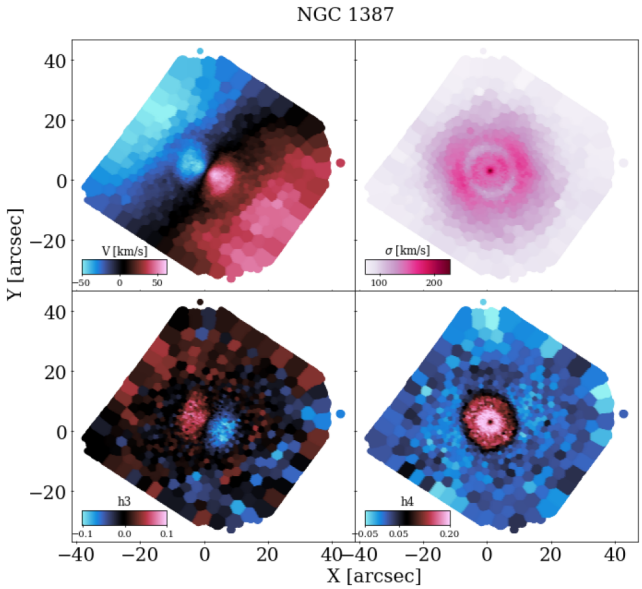

Figure 2. Kinematic properties of the stellar component of NGC 1387 as obtained with GIST.

4 DETECTING PLANETARY NEBULAE

4.1 Detecting and measuring the [O III] 5007Å emission line

As mentioned above, the main issue we face when it comes to detecting emission lines from unresolved PNe in the inner region of galaxies is the intensity of the stellar continuum. We followed the approach described by M. M. Roth et al. (2021), creating a continuum

[3] We are aware that for the most massive ones ETGs, the IMF could be dwarf-richer. However, below < 6000 Å, the contribution of IMF variations is almost negligible.

[4] Equivalent figures for the other nine galaxies in the sample are presented in Appendix A.

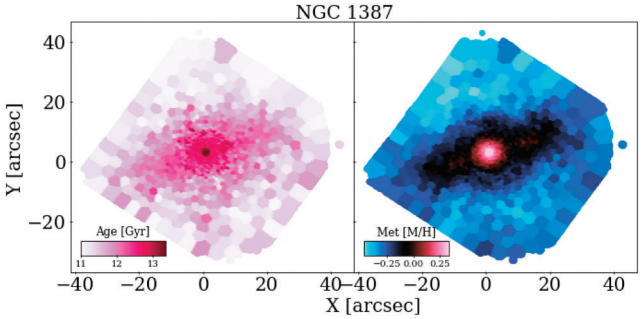

Figure 3. Age and metallicity of the stellar component of NGC 1387 as obtained with GIST.

image by co-adding layers from the cube redward of the redshifted [O III] 5007Å line.

The DELF method makes use of the high spectral resolution in MUSE data cubes to extract images with a very narrow spectral range, which reduces systematic noise. Splitting the narrow-band filter in this manner increases the SNR of the emission lines, facilitating the detection of fainter objects even in the central regions.

We extracted 15 slices with the shortest spectral range possible given the spectral resolution available (1.25 Å), from which we subtract the scaled continuum image to obtain *diff* images. These slices are centred in the redshifted position of the [O III] 5007Å line, and they cover the expected range of radial velocities for PNe in the centres of ETGs, $\pm 500\,\mathrm{km\,s^{-1}}$. Considering the typical spectral FWHM in MUSE data, ~ 2.6 Å, we expect emission lines to take up at least three slices. To enhance the detection of faint objects, we built narrow-band images by adding up to three consecutive slices, thus increasing the flux in the emission line. Using SEXTRACTOR (E. Bertin & S. Arnouts 1996), we detected the point-like sources present in each of these images, considering as positive detections those that appear in at least three adjacent images (see also M. M. Roth et al. 2021). Since there is still a significant amount of noise in these images, we used the variance maps as weight images to avoid spurious detections.

We obtained the aperture magnitude for each of our detected sources in each slice, using an aperture of 5 pixels and creating a short spectrum as shown in Fig. 4. We fitted a Gaussian profile to this short spectrum as a way to automatically reject any remaining spurious detections. These are mainly sources where there is extended emission or where an issue in the continuum generates a false detection, such as groups of pixels in the edge of the field with arbitrarily negative and positive values. In these short spectra, the continuum subtraction presents some issues that generate noise in the calculation of the flux. In order to obtain more accurate magnitudes, we obtained the aperture photometry of every single slice throughout the entire spectra of each source, using the original cube. We defined an annulus around each

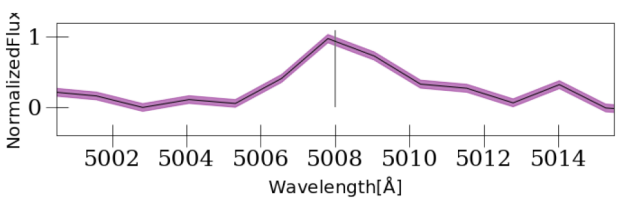

Figure 4. Zoom-in on the region of the [O III] line using the spectra constructed from the aperture photometry method described in the text. A grey vertical line indicates the rest-frame wavelength in air of the [O III] line.

source when performing aperture photometry from which the sky is measured locally. Subtracting this value from the flux measured in the source resulted in a cleaner continuum subtraction. Through this process, we computed a measurement of the flux in every slice of the spectrum, which allows to obtain the total flux of the line, F_{5007}, by adding the flux measured in each slice, obtaining the spectra shown in Fig. 5. We apply an aperture correction to these flux measurements. We then calculated the magnitude of the line following the Jacoby relation (1989):

$$m_{5007} = -2.5\,\mathrm{logF}_{5007} - 13.74. \quad (4)$$

The magnitudes obtained in this way are compatible with the ones resulting from the integration of the Gaussian profile fitted to the short spectrum, but the errors are smaller using aperture photometry, and this method is much more efficient when applied to faint objects than the integration of the line. The spectrum obtained in this manner is show in Figs 4 and 5 for the case of NGC 1387.

4.2 Detecting interlopers

The next step is to identify interlopers (e.g. other sources that can be detected in the [O III] 5007Å filters) in our catalogue by first measuring the flux of other emission lines and then applying cuts based on established emission-line ratios. In order to do this, we extracted the spectra corresponding to each detection using aperture photometry throughout the entire continuum-subtracted cube. This allowed us to identify emission lines typically used in diagnostic diagrams, and to measure their flux using the same method as described for [O III]. The most common interlopers are mainly H II regions and supernovae remnants.

Ly α emitters and other background galaxies at high redshift may also show up in narrow-band surveys because their lines can be redshifted into the bandpass. However, background galaxies are easily distinguishable from PNe in MUSE data since they present multiple emission lines, and the Ly α line has a characteristic profile through which it can be identified. The [O III] line is a doublet (4959Å, 5007Å), which can also be used to confirm the emission that is being detected, though the second line is fainter and therefore harder to detect.

H II regions and PNe both emit Hα and [O III] lines, but the ratio [O III]/H α tends to differ. In H II regions, the Hα emission is usually more intense than emission in the [O III] doublet (P. A. Shaver et al. 1983), while the opposite happens in PNe spectra (J. A. Baldwin, M. M. Phillips & R. Terlevich 1981). In particular, R. Ciardullo et al. (2002) found that the typical ratios of emission lines in PNe can be described with the following equation:

$$4 > \log \frac{[\mathrm{O\,iii}]}{\mathrm{H}\alpha + [\mathrm{N\,ii}]} > -0.37\,\mathrm{M}_{[\mathrm{O\,iii}]} - 1.16 \quad (5)$$

In Fig. 6 we show our diagnostic diagram for NGC 1387, with the relations from equation (5) plotted with solid lines. The diagnostic diagrams for the entire sample can be found in Appendix B. The applied criterion is empirical, and though there are others based on spectroscopy, we consider it is enough for our sample based on K. Kreckel et al. (2017).

Notably, the region of the diagram where the ratio of emission lines is $\log \frac{[\mathrm{O\,iii}]}{\mathrm{H}\alpha\,[\mathrm{N\,ii}]} > 4$ shows several sources for many of our galaxies. Due to measurement errors, some of the objects in this region could be genuine PNe, however, after careful inspection of the spectra, we cannot say this with certainty for all objects above the line. We therefore only consider the objects within the regions defined by

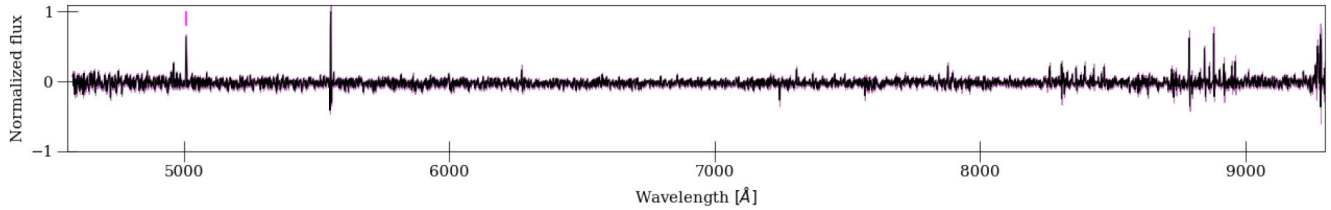

Figure 5. Full MUSE spectrum for one of the sources classified as PNe in NGC 1387. A vertical line indicates the position of the [O III] line].

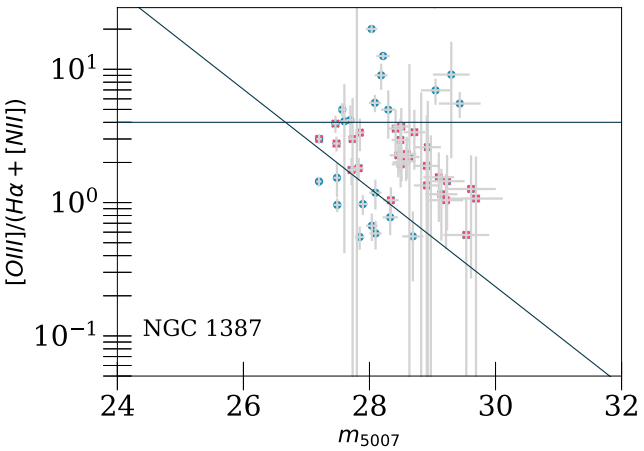

Figure 6. [O iii]/(Hα + [N ii]) line ratios as a function of [O III] apparent magnitude for the entire sample of objects detected in NGC 1387 using the [O III] field. The solid lines indicate the criteria that separate PNe candidates (dots that fall between the lines) from contaminants (dots above the horizontal line or below the diagonal) following R. Ciardullo et al. (2002).

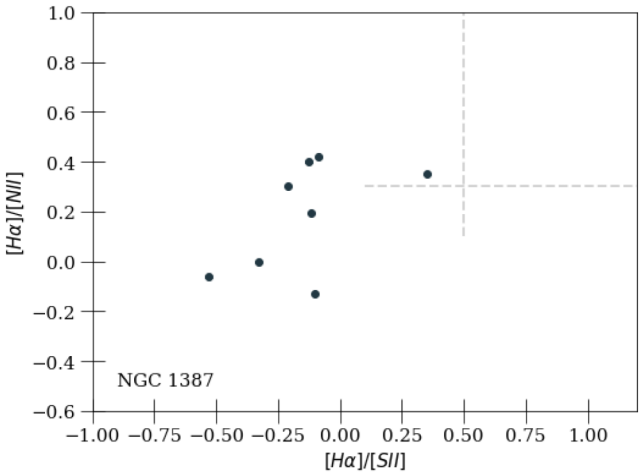

Figure 7. Hα/[N ii] as a function of Hα/[S ii] for all sources detected in the [O III] filter in NGC 1387. The black dots indicate sources likely to be supernovae remnants. The dashed lines separate the area where H II regions would be found, following the criteria from F. Sabbadin et al. (1977).

Equation 5 as bona fide PNe and note that the total number of PNe could be underestimated by a factor of 1.1–1.7.

For sources considered interlopers or contaminants, we can analyse other line ratios in order to discriminate H II regions from supernovae remnants. For objects in which [N II] and [S II] lines are strong enough, we follow the analysis proposed originally by F. Sabbadin, S. Minello & A. Bianchini (1977). In Fig. 7 we show the distribution of the interlopers found in the NGC 1387 sample with

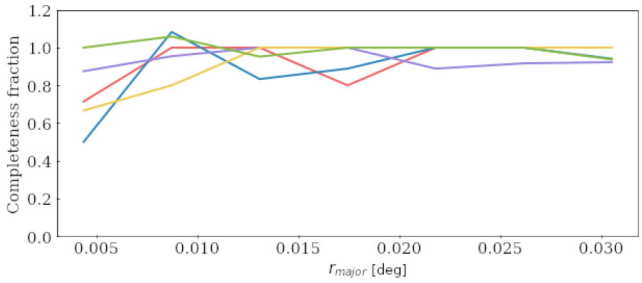

Figure 8. Completeness fraction of several slices in NGC 1387 in relation to the distance to the galactic centre.

strong [N II] and [S II] lines. All of these objects have line ratios consistent with supernovae remnants. Considering we are looking at the central region of an ETG, it is not unexpected that we find no H II regions, which are more common in LTGs with younger populations and ongoing star formation. Our catalogue for NGC 1387, which started with 63 candidates detected via the DELF technique, is then composed of 26 PNe, with a magnitude range $29.8 < m_{5007} < 27.5$.

4.3 Completeness test

Estimating the completeness is necessary for the derivation of the PNLF, and also for the analysis of the PN number density profile. Since we are attempting to recover faint objects from a crowded area with a strong continuum, it is indispensable to obtain accurate completeness levels, both in terms of magnitude and of isophotal galactocentric distance.

We built 20 catalogues of $\sim$ 100 sources each for which we create a position and a magnitude considering the size and shape of each FoV and a magnitude range of $m_* - m_{\rm lim} = 3$, where m_* is the bright cut-off estimated from the SBF distance for each galaxy. We used tasks from PHOTUTILS.DATASETS to add the objects to our [O III] image where we performed the detections, using an elliptical Moffat profile with standard parameters simulating the PSF of MUSE to shape the sources.

We then repeated the detection process previously described for PNe candidates and compared the fraction of recovery of sources in relation to the isophotal galactocentric distance and the [O III] line magnitude. For our pilot case, NGC 1387, we performed this process for each slice separately. Since the trends are comparable across all slices, showing no dependence with wavelength, we performed the process based on a single slice for the remaining galaxies in the sample. In Figs 8 and 9, we show the completeness fractions corresponding to several slices in NGC 1387 in relation to distance and magnitude. The inner regions present the lowest values of completeness, which is expected due to the brightness of the stellar component increasing towards the centre. In terms of magnitude, the completeness fraction decreases towards the faint end.

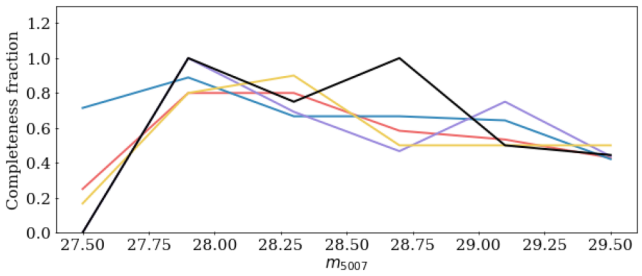

Figure 9. Completeness fraction of several slices in NGC 1387 in relation to the magnitude of their [O III] line.

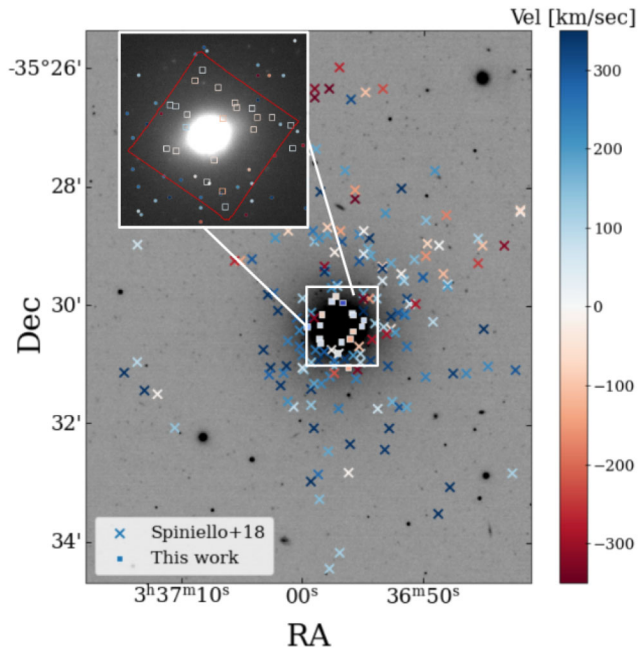

Figure 10. PNe detected in NGC 1387 overlaid on a DSS2 image of the galaxy. The crosses represent the sample by C. Spiniello et al. (2018), and squares, our detections, filling the previous blind spot. The zoomed-in square on the top left highlights our sample, with squares for our sample and circles for the previous catalogue. The square marks the shape of the MUSE data cube. The colourbar represents the kinematics of the PNe.

5 PLANETARY NEBULAE ANALYSIS

5.1 Spatial distribution and kinematics

In Fig. 10, we show the PNe catalogue obtained for NGC 1387 by C. Spiniello et al. (2018), combined with our PNe detections. C. Spiniello et al. (2018) obtained their sample from VLT-FORS2 observations, using the inverse-dispersion method (N. G. Douglas & K. Taylor 1999). The observed MUSE field is situated in the central region, where the classical method presents a clear blind spot. In the case of NGC 1387, this $1' \times 1'$ region is approximately $5 \times 5\,\mathrm{kpc}^2$. There are seven sources in C. Spiniello et al. (2018) that fall in the edges of our field, and are therefore not detected. Four others fall inside the field, near the edges, and are too weak for our completeness limit. One source is common to both catalogues. We do not incorporate the missing sources to our analysis for consistency since we cannot do this with the rest of the sample.

From the [O III] 5007Å line shift, we obtain the velocity for each PNe, thus obtaining the velocity distribution shown in Fig. 10. The PN velocities are consistent with the velocity dispersion and systemic velocity derived from absorption spectroscopy. Future work will link the stellar and PN kinematics with those at large radii as traced by C. Spiniello et al. (2018).

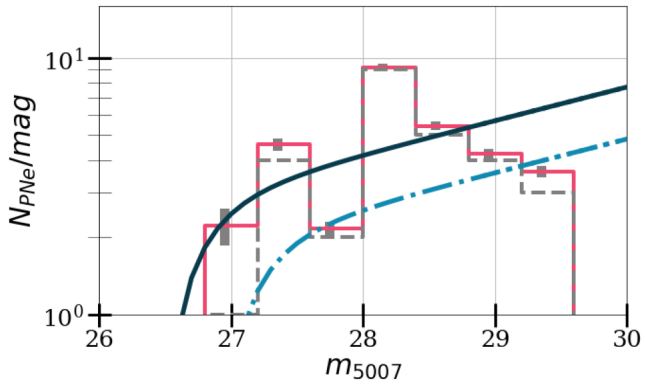

Figure 11. The grey dashed histogram shows the observed PNLF for NGC 1387, and in solid lines we show the version corrected by completeness, with thick bars indicating the errors. The dash–dotted curve shows the best-fitting analytic PNLF with a fixed bright cut-off based on the galaxy's distance, and the solid line indicates the function resulting from fitting the bright-cut off to our data.

5.2 Luminosity function

The PNLF quantifies the number of PNe in terms of the magnitude of the [O III] 5007 Å line, which is obtained following equation (4). The analytic fit to the PNLF was first determined for the bulge of M31 (R. Ciardullo et al. 1989), and has ever since proven to have a near universal shape following equation (1).

Due to the small size of the FoV and the fact that our observed PNLFs are only complete to 1–2 mag from the bright cut-off M^*, we refrain from analysing the variation of the slope in this work, and instead use the 'traditional' R. Ciardullo et al. (1989) PNLF with $c_2 = 0.307$. The main purpose of the PNLF in this analysis is to extrapolate our sample to a homogeneous limit in the faint end. As shown in Fig. 11, we fit two versions of the function, one with a variable bright cut-off and one with this value fixed according to the SBF distance to the galaxy, to the completeness-corrected observed PNLF. This is done for comparison purposes, but to facilitate cross-galaxy comparison, we perform the following extrapolations using the function with the fixed cut-off, fitting only the normalization c_1. From Fig. 11, we can evaluate already that the sensitivity reached by the MUSE data is $\Delta m \sim 2$–2.5 below the PNLF bright cut-off.

5.3 Surface brightness profile of galaxies and PNe number density

As PNe trace the stellar populations of ETGs, their number density profile is expected to be proportional to the surface brightness profile of elliptical (L. Coccato et al. 2009; A. Longobardi et al. 2013) and lenticular galaxies (A. Cortesi et al. 2013a,b).

For galaxies for which we have data with the FoV of a single MUSE cube, we generate a wide-band image from our data cubes in the Cousins V filter using the MUSE pipeline. We then use tasks from STATMORPH (V. Rodriguez-Gomez et al. 2019) to fit a Sérsic profile (J. L. Sersic 1968) to the brightness distribution of the galaxy. For the closest galaxies in our sample, where we have a mosaic of several cubes, sometimes with different sensitivities, we use surface

Table 2. Literature references for galaxies whose surface brightness profile we did not measure ourselves.

Galaxy	Reference
NGC 1387	Z.-Y. Li et al. (2011)
NGC 1404	Z.-Y. Li et al. (2011)
NGC 1399	N. Caon, M. Capaccioli & M. D'Onofrio (1994)
NGC 3115	M. Capaccioli, E. V. Held & J.-L. Nieto (1987)
NGC 3379	A. E. Watkins et al. (2014), M. G. Lee & I. S. Jang (2016), J. Hartke et al. (2020)
NGC 4365	J. Kormendy et al. (2009)
NGC 4374	J. Kormendy et al. (2009)
NGC 4472	J. Kormendy et al. (2009)
NGC 4594	Z.-Y. Li et al. (2011)
NGC 5128	Z.-Y. Li et al. (2011)

brightness profiles obtained from the literature (all references listed in Table 2), and fit Sérsic profiles to them.

The number density profile of our PNe samples is obtained by splitting the area into concentric regions, and dividing the amount of PNe detected in each of these regions by its area. The PNe density profile is defined as

$$\mu_{\rm PN}(r) = -2.5\ \log_{10}\Sigma_{\rm PN}(r) + \mu_0, \tag{6}$$

where μ_0 is a constant that we fit to relate the observed PN number density with the stellar surface brightness, and $\Sigma_{\rm PN}$ is the PNe number density, corrected by spatial completeness and limited in magnitude by the brightness completeness.

As the α-parameter relates the number of PNe with the total luminosity of a galaxy, we first need a bolometric correction, which, following B06, is defined as

$$I = 10^{-0.4(BC_V - BC_\odot)}10^{-0.4(\mu - K)}, \tag{7}$$

$BC_\odot$ is the solar bolometric correction and BC_V is the bolometric correction for a stellar population model using the V filter, which can be assumed to have a fixed value of -0.85 with 10 per cent accuracy (B06). K is the conversion factor from the units of surface brightness in the chosen band to the physical units $L_\odot {\rm pc}^{-2}$, defined as $K = M_{\odot,\rm filter} + 21.572$.[5] We then calculate the α-parameter using the following equation:

$$\alpha = \frac{10^{-0.4(\mu_0 - K - (BC_\odot - BC_V))}}{s^2}, \tag{8}$$

where $s = D/206265$ is a scale factor related to the distance to the galaxy, D. For NGC 1387, we obtain $\mu_0 = 18.14 \pm 0.4$ mag and $\alpha = (3.25 \pm 1.88) \times 10^{-8}$ PN $L_{\rm BOL}^{-1}$. Fig. 12 shows the result of offsetting the PNe density profile by this value of μ_0. From this fit, we can calculate the α-parameter. Although we perform a correction for the area not covered by the annuli in which we measure the PNe density, we exclude annuli for which either the completeness or the covered area is less than 50 per cent when we perform the fit to measure the offset. Points excluded are shown as black dots in the plots or are excluded from the range displayed. We consider the α-parameter as $\alpha_{2.5}$, meaning our magnitudes are between the bright cut-off, m_*, and $m_* + 2.5$, as shown previously in Fig. 11. This is done for homogeneity, since the completeness levels vary through the sample, and to facilitate future comparisons.

Since completeness limits vary for each galaxy, and in order to obtain a value more directly comparable to the literature, we consider

[5] https://web.archive.org/web/20070718015507www.ucolick.org/~cnaw/sun.html

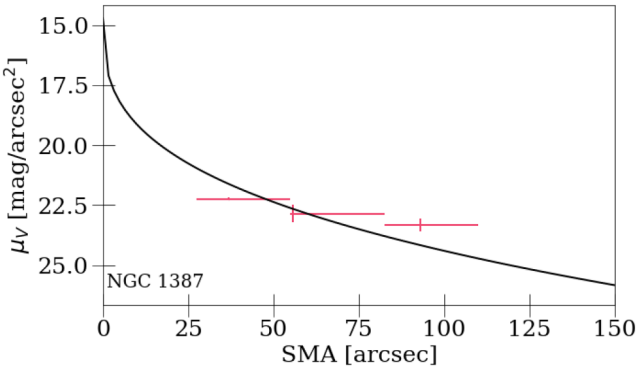

Figure 12. Sérsic fit to the surface brightness profile for NGC 1387 in the V-band shown in solid line. The crosses indicate the PNe density offset by the fitted constant μ_0, with the errorbars indicating the size of the bin in the x-axis and the density error in the y-axis.

a magnitude range of $\Delta m = 2.5$ mag from the bright cut-off. In the case of NGC 1387, our completeness limit is $m = 29$, which is half a magnitude fainter. From the PNLF we can obtain the difference between these magnitude ranges, following

$$\Delta m_c = \frac{\int_{m*}^{m*+2.5} N(m){\rm d}m}{\int_{m*}^{m_c} N(m){\rm d}m} \tag{9}$$

This allows us to extrapolate and to obtain $\alpha_{2.5}$, with $\alpha_{2.5} = \Delta m_c \times \alpha_{m_c}$. This results in $\alpha_{2.5} = (4.32 \pm 2.49) \times 10^{-8}$ PN $L_{\rm BOL}^{-1}$ for NGC 1387. A summary of the α-parameters for all galaxies in the sample, as well as the results from the stellar population analysis, can be found in Table 3.

6 DISCUSSION

6.1 Comparison with existing catalogues

Three of the galaxies in our sample, NGC 1399, NGC 1404, and NGC 4472, were previously studied in G. H. Jacoby et al. (2024), using the DELF method but performing the detection of sources visually, blinking through the slices. These three particular cubes each have their own challenges. The version available in the archive of the reduced mosaic for NGC 1399, as shown in G. H. Jacoby et al. (2024), presents an imperfect flat-field corrections and the noise varies significantly across the galaxy. In the case of NGC 1404, there are two available cubes, which we analyse individually and then combine, whereas G. H. Jacoby et al. (2024) reduce the data from scratch. Finally, NGC 4472 has the shortest exposure times in both samples, resulting in very shallow cubes. For the latter cases, we recover approximately half the sources present in the previous work, and some new ones. For NGC 1399, we find nine PNe, in stark contrast to the over 100 found in G. H. Jacoby et al. (2024). It is expected that we should find less sources with an automated detection mechanism, and it is particularly challenging for the spatially variable background for emission lines, as mentioned by A. A. Soemitro et al. (2023a). In our case, the initial detection finds up to 70 per cent of the sources in the previous catalogues. Interestingly, most of them do not meet our criteria when fitting a Gaussian to the emission line, and some are not considered PNe when evaluating the diagnostic diagrams.

Table 3. Mean values of the stellar population properties obtained from GIST, and α-parameter up to 2.5 mag from the bright cut-off of the PNLF for the entire sample.

Galaxy	Age (Gyr)	(Fe/H)	σ (km s^{-1})	α ($\times 10^9$)	$\alpha_{\rm err}$ ($\times 10^9$)
NGC 1387	11.5 ± 0.4	-0.29 ± 0.09	102.62 ± 20.23	11.66	11.71
NGC 1399	12.3 ± 0.7	-0.11 ± 0.29	229.88 ± 10.51	1.47	1.37
NGC 1404	12.7 ± 0.3	-0.08 ± 0.10	189.87 ± 18.96	4.82	2.14
NGC 3115	10.9 ± 1.3	-0.08 ± 0.17	123.95 ± 26.76	4.55	1.55
NGC 3379	12.7 ± 0.6	-0.12 ± 0.14	159.05 ± 30.79	3.22	0.98
NGC 4365	11.4 ± 0.9	0.14 ± 0.09	233.39 ± 10.38	2.12	0.37
NGC 4374	12.7 ± 0.2	0.00 ± 0.07	276.97 ± 6.76	1.10	1.19
NGC 4472	9.1 ± 1.4	-0.44 ± 0.05	257.26 ± 62.54	4.19	8.24
NGC 4594	8.3 ± 2.5	-0.11 ± 0.22	196.84 ± 60.08	6.36	1.66
NGC 5128	4.6 ± 1.4	-0.77 ± 0.52	191.73 ± 92.78	7.08	1.07

6.2 The luminosity-specific PN number as tracer of stellar population properties

The starting point of the original analysis done in B06 regarding the α-parameter is Fig. 10 therein, which shows its variation in relation to the colour of the host galaxy both in observations and in models. LTG on the blue end have, on average, higher observed α-parameter values than red ellipticals, which, however, present a larger scatter. This relation with colour has been shown to remain true when considering different components of a single galaxy, e.g. in M87 (A. Longobardi et al. 2013), where the inner red halo has a lower α value that increases in the outer bluer region. This is seen as well in M49 (J. Hartke et al. 2017), in M31 (S. Bhattacharya et al. 2019), and in M105 (J. Hartke et al. 2020), where the α-parameter is shown to be tracing distinct populations across the entire radial extent of a galaxy.

Fig. 13 shows the relation between $\alpha_{2.5}$ and the $(B-V)$ colour of the host galaxy for the B06 galaxies and our sample, as obtained from G. Vaucouleurs et al. (1991) for NGC 3379, NGC 4365, NGC 4374, and NGC 4472, and from L. C. Ho et al. (2011) for the rest of the sample, both corrected for extinction. The colour bar indicates the mean of the metallicity of the stellar population. Our sample of galaxies follows the relation, although with some scatter. In Fig. 14, we show the relation between $\alpha_{2.5}$ and the mean metallicity of the corresponding data cube for its host galaxy. Most galaxies in the sample follow the relation traced by M105, minus the previously described outliers that fall well below it. From Fig. 15, which shows the relation between $\alpha_{2.5}$ and the age of the host galaxy, it seems clear that metallicity is driving the correlation seen in colour. Recent theoretical results from L. M. Valenzuela et al. (2025) find a strong correlation of $\alpha_{2.5}$ with metallicity and a weaker one with age, although similarly to previous results in B06, the theoretical correlation would predict an exact opposite trend to the one obtained observationally, with higher predicted values of $\alpha_{2.5}$ in galaxies with higher metallicities.

It is noteworthy that the relation between the α-parameter and colour or metallicity are much more prominent in the studies of individual galaxies, i.e. M49 and M105. In both of these cases, the comparison is performed between distinct halo populations with less weaker age and metallicity gradients than the stellar cores studied in this work.

Finally, Fig. 16 shows the relation between $\alpha_{2.5}$ and the velocity dispersion as measured at the centre of the galaxy. It can be argued that the relation shown in B06 where higher velocity dispersions correspond to lower number densities prevails in this sample. This in turn may be interpreted as a relation between $\alpha_{2.5}$ and the total mass of the galaxy.

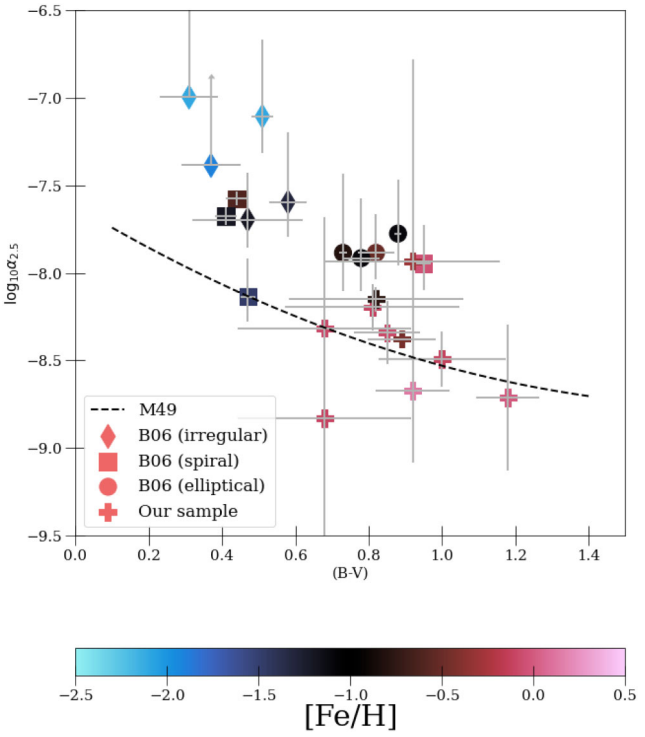

Figure 13. Luminosity-specific PN number $\alpha_{2.5}$ versus the $(B-V)$ colour of the host galaxy, coloured by the metallicity of the galaxy. The thick crosses indicate our sample. The dashed line indicates the results for M49 obtained by J. Hartke et al. (2017).

6.3 PNe visibility lifetime

The α-parameter is defined as $\alpha = {\rm N_{PN}}/{\rm L_{bol}}$, where the number of observable PNe, $\rm N_{PN}$, depends on the evolutionary flux $\mathcal{B}$ of and the visibility lifetime $\tau_{\rm PN}$ according to the SSP theory developed by A. Renzini & A. Buzzoni (1986) and A. Buzzoni (1989). A lower value of α may then be a result of shorter PN lifetimes, which may be due to evolutionary reasons linked to the properties of the stellar populations, or to the interaction of the interstellar medium with the PN envelopes. In the central regions of massive ETGs, hot gas in high densities could cause ram-pressure stripping of the envelopes, effectively reducing $\tau_{\rm PN}$ (M. A. Dopita et al. 2000; J. Martin, K. Xilouris & N. Soker 2002; E. Villaver & L. Stanghellini 2005). However, in Fig. 17 no clear correlation is seen between the intensity of the X-ray emission in the central region of the galaxies and the α

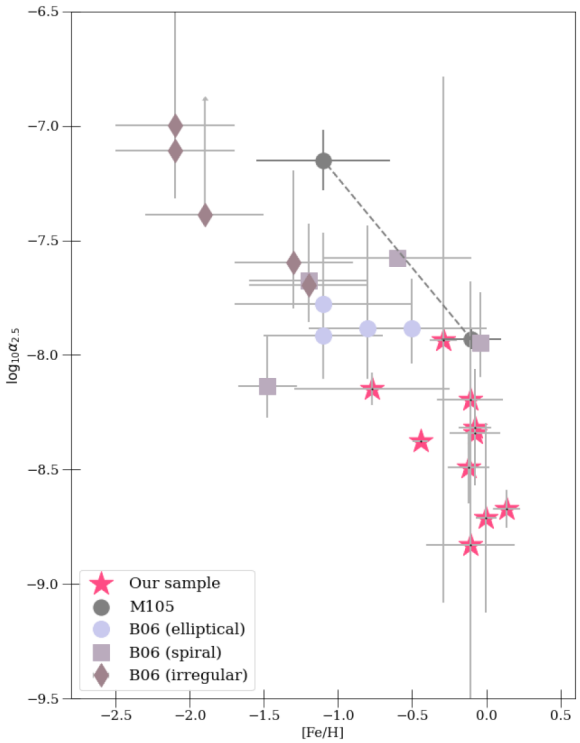

Figure 14. Luminosity-specific PN number $\alpha_{2.5}$ versus the metallicity of the galaxy for the B06 sample in pastel colours. The stars show the results from our sample. The dots joined by a dashed line show the results from J. Hartke et al. (2022) for M105.

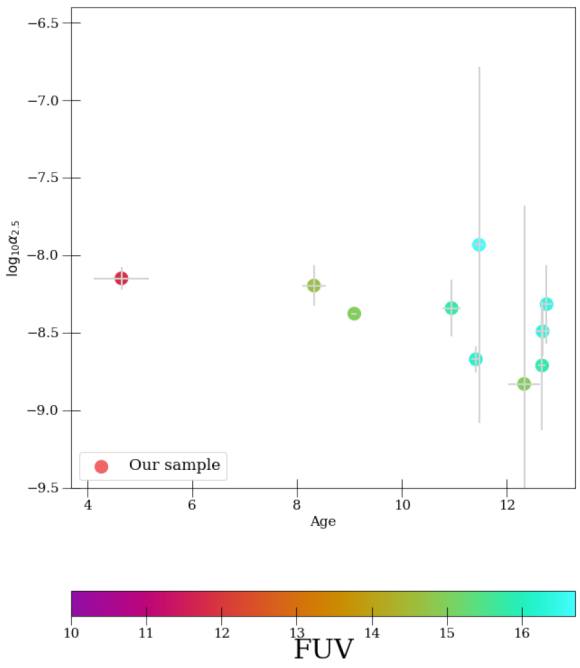

Figure 15. Luminosity-specific PN number $\alpha_{2.5}$ versus the age of the host galaxy for the galaxies in our sample.

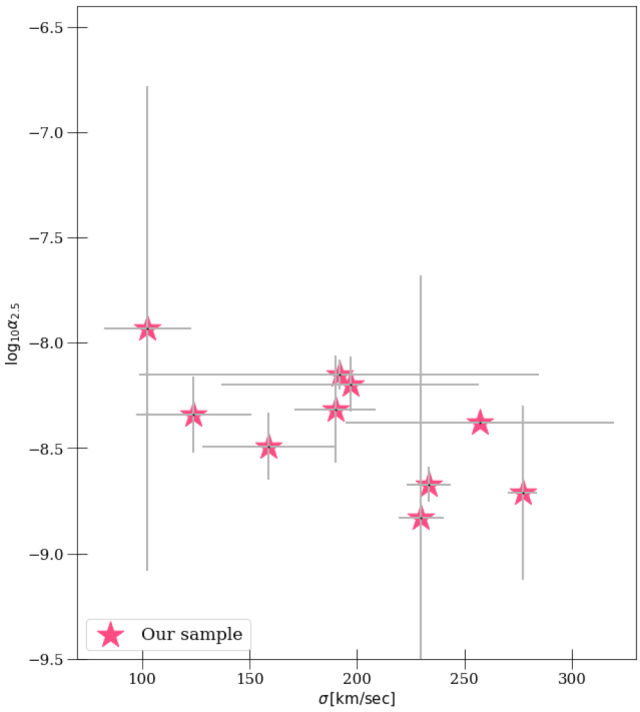

Figure 16. Luminosity-specific PN number $\alpha_{2.5}$ versus the velocity dispersion of the host galaxy for the galaxies in our sample.

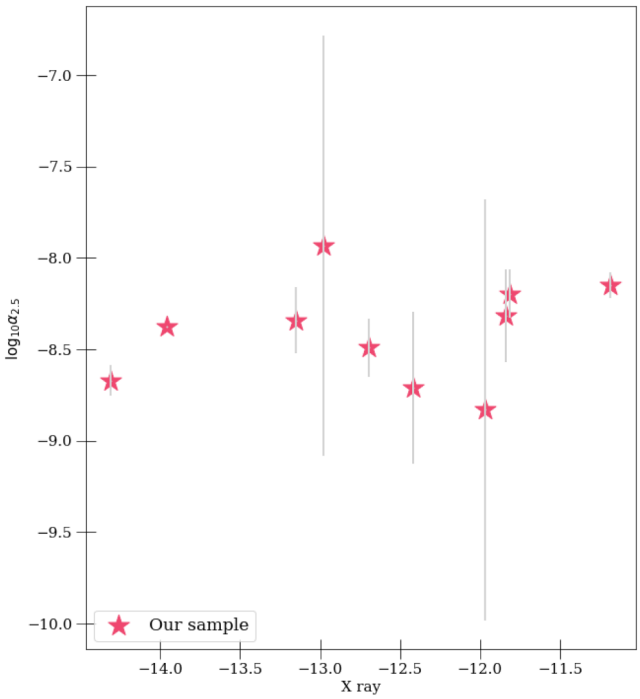

Figure 17. Luminosity-specific PN number $\alpha_{2.5}$ versus the X-ray magnitude of the host galaxy for the galaxies in our sample.

parameter within the current sample. The X-ray values used in this analysis are reported in Table 4.

In a different wavelength range, the UV excess has been shown to anticorrelate with α (B06), and in more detail in R. Ciardullo et al. (2005), using $m_{1500} - V$, which has a dynamic range six times larger than FUV–NUV. The evolutionary pathways of stars are nuanced,

Table 4. UV magnitudes and X-ray fluxes for the central regions of each galaxy obtained from the literature. FUV and NUV were obtained from Y. Bai et al. (2015) for galaxies signalled as [1] and D. Zaritsky, A. Gil de Paz & A. Y. K. Bouquin (2015) for [2], which are corrected for Galactic extinction using the Galactic Reddening Map of D. J. Schlegel, D. P. Finkbeiner & M. Davis (1998) and the reddening law of J. A. Cardelli, G. C. Clayton & J. S. Mathis (1989). X-ray magnitudes are from I. V. Babyk et al. (2018) except for NGC 3115 (M. A. Norris, R. M. Sharples & H. Kuntschner 2006) and NGC 4594 (O. González-Martín et al. 2009). We found no values in the literature for NGC 1387 and NGC 5128.

Galaxy	FUV (mag)	NUV (mag)	$\log_{10}$(X-ray[erg cm^{-2} s^{-1}])
NGC 1387[1]	16.71 ± 0.05	15.75 ± 0.07	N/A
NGC 1399[1]	14.96 ± 0.05	14.31 ± 0.03	-11.30 ± 0.002
NGC 1404[1]	16.37 ± 0.05	15.21 ± 0.03	-11.54 ± 0.002
NGC 3115[1]	15.78 ± 0.14	14.34 ± 0.02	-12.83 ± 0.003
NGC 3379[1]	16.33 ± 0.03	14.91 ± 0.02	-13.31 ± 0.05
NGC 4365[2]	16.18 ± 0.02	14.93 ± 0.02	-12.97 ± 0.002
NGC 4374[1]	15.82 ± 0.13	14.40 ± 0.05	-11.85 ± 0.004
NGC 4472[1]	14.98 ± 0.03	13.99 ± 0.02	-11.30 ± 0.002
NGC 4594[2]	14.68 ± 0.11	13.36 ± 0.06	-12.60 ± 0.003
NGC 5128[1]	11.83 ± 0.07	10.47 ± 0.13	N/A

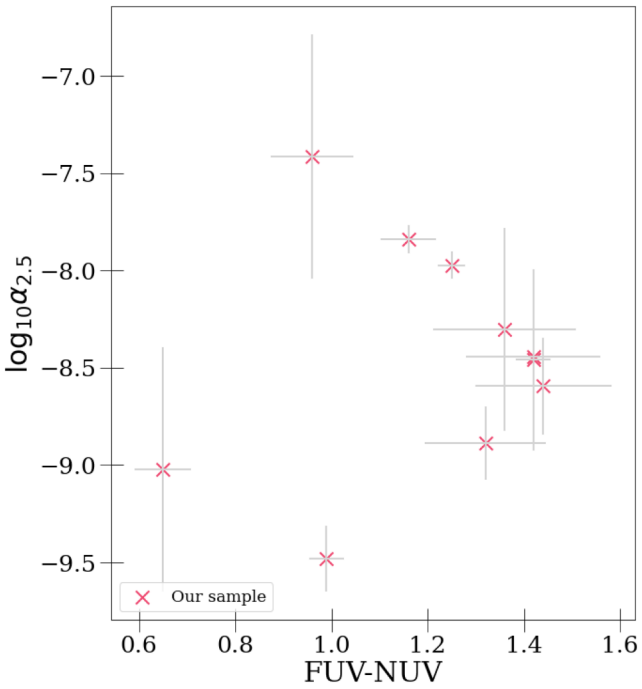

Figure 18. Luminosity-specific PN number $\alpha_{2.5}$ versus FUV–NUV colour of the host galaxy for the galaxies in our sample.

and the visibility lifetime of a PNe is very dependent on how hot the core is, and on the asymptotic giant branch transition time. Stars with low-mass cores occupy the hotter horizontal branch, and skip the PNe phase since the envelope fades very quickly. This affects the spectral energy distribution of the galaxy, resulting in UV-enhanced ellipticals being expected to haver lower α values. In Fig. 18 we show that this anticorrelation is present in our sample despite the scatter. An outlier in the $\log\alpha_{2.5}$ versus FUV–NUV plot, NGC 1399, place in the lower left corner, disrupts the contour of the proposed anticorrelation. NGC 1399 is a complex galaxy, and in future work we will analyse its α-parameter and its potential variations, studying the effects of active galactic nucleus (AGN) activity on PNe populations. Expanding our sample beyond ETGs and performing the observations and analysis in a systematic way will provide a stronger conclusion.

Finally, Fig. 19 shows a corner plot with all the analysed parameters in order to visualize all relations. From this Figure, we see there although there is scatter, there is a correlation between $\alpha_{2.5}$ and metallicity, as well with the FUV excess.

6.4 Limitations and prospects of archival data

Astronomers currently have access to unprecedented amounts of high-quality data, made available through careful upkeeping of observatory archives. Although archival data are a precious tool that allows for works such as this one, providing the possibility to test pipelines and methods on large data sets with varying quality, it comes with limitations due to the mix of observing conditions, mainly caused by the different research questions behind the original proposals.

As mentioned, IFU spectroscopy enables detecting PNe in regions where previous methods faced insurmountable challenges. However, several considerations must be made even with this powerful tool at hand. Galaxies with AGNs, such as NGC 1316, proved immune to the method, since the emission lines of the AGNs were too intense and widespread across the cubes to untangle them from PNe candidates. Galaxies at smaller distances, such as NGC 5128, occupy an FoV that requires constructing a mosaic from several pointings, which is expensive in telescope time despite the shorter exposure time per pointing and may result in varying depths across the field. Finally, characterizing the age and metallicity of the stellar component is highly challenging in galaxies with dusty centres, as seen in NGC 5128 as well as NGC 4594. For future work, an ideal sample should be observed considering the needed sensitivity to reach the $m^* + 2.5$ limit in the [O III] 5007Å line as to avoid extrapolating, focusing on ETGs between 15 and 25 Mpc. To apply this method, both the spatial and spectral resolution are highly relevant. The spectral sampling of MUSE, 1.25Å, is key for DELF to work, and similar or higher spectral resolutions should be aimed for also in future works, keeping in mind that increasing the spectral resolution too much would resolve the emission lines and hinder the process rather than help it. Spatially, the method relies on detecting PNe as point-like sources, which implies a constraint on image quality according to the distance of the host galaxy. In the case of MUSE, using its adaptive optics system may significantly boost PN detections (e.g. A. A. Soemitro et al. 2023b). Finally, the BlueMUSE instrument (J. Richard et al. 2019) with a similar instrument design compared to MUSE, but with a larger FoV and a bluer spectral coverage will also allow direct abundance determinations of extragalactic PNe in the centres of galaxies.

7 SUMMARY AND CONCLUSIONS

In this work, we analyse the central regions of a sample of 10 ETGs, detecting and identifying PNe using MUSE archival data. We focus on the α-parameter, i.e. the luminosity-specific number density of PNe, and its potential correlations with a variety of properties of the underlying stellar population. We find that the α-parameter remains tightly constrained within a narrow range of values, as shown for galaxy haloes across the literature. Our sample of galaxies follows the previously proposed correlation between the α-parameter and the metallicity of the host galaxies, while the correlation with age is very weak, implying the correlation with colour shown in B06 is possibly driven by the metallicity of the underlying subpopulations. The

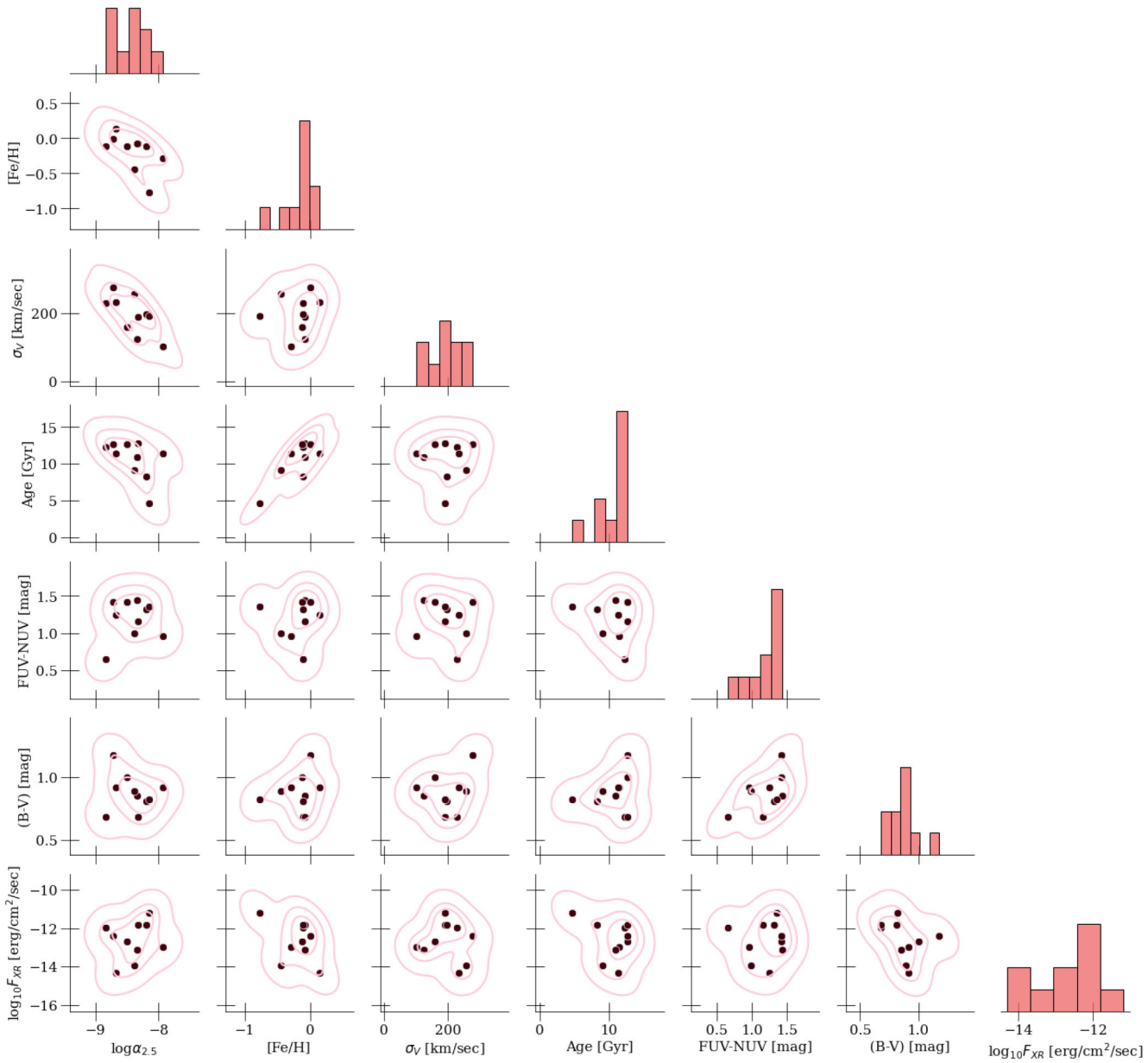

Figure 19. Corner plot showing the relations between all analysed parameters. Measurements are in black points, with solid pink lines indicating density estimations obtained with KDE. The upper plots show histograms corresponding to each parameter.

FUV excess anticorrelates with the α-parameter, validating previous results and confirming a tension between theoretical predictions and observed PN population properties, despite inclusion of then most recent advanced PAGB evolution tracks. A larger sample is required for future work to confirm these results and further improve our understanding of the physics behind these relations.

ACKNOWLEDGEMENTS

We thank the referee for an insightful report and helpful comments that improved this work. We thank Martin Roth for providing guidance for using DELF. We thank Felipe Gran for sharing part of the code used to perform aperture photometry on the cubes. We also thank Elizaveta Sazonova for useful discussions and suggestions. This research was supported in part by Perimeter Institute for Theoretical Physics. Research at Perimeter Institute is supported by the Government of Canada through the Department of Innovation, Science and Economic Development and by the Province of Ontario through the Ministry of Research and Innovation. AE and JH acknowledge the financial support from the visitor programme of the Finnish Centre for Astronomy with ESO (FINCA), funded by the Academy of Finland grant no. 306531. This work made use of AstroPy (Astropy Collaboration 2013, 2018, 2022), Matplotlib (J. D. Hunter 2007), NumPy (C. R. Harris et al. 2020) Pandas (W. McKinney 2010), PhotUtils (L. Bradley et al. 2023), SciKit (F. Pedregosa et al. 2011) and SciPy (P. Virtanen et al. 2020).

DATA AVAILABILITY

The processed MUSE data are all publicly available from the ESO Science Archive (DOI: https://doi.eso.org/10.18727/archive/41) We plan to release our PN catalogues as advanced data products to ESO.

REFERENCES

Annibali F. et al., 2017, ApJ, 843, 20
Arnaboldi M. et al., 1996, ApJ, 472, 145
Arnaboldi M., Gerhard O., 2022, Front. Astron. Space Sci., 9, 403
Astropy Collaboration, 2013, A&A, 558, A33
Astropy Collaboration, 2018, AJ, 156, 123
Astropy Collaboration, 2022, ApJ, 935, 167
Babyk I. V., McNamara B. R., Nulsen P. E. J., Hogan M. T., Vantyghem A. N., Russell H. R., Pulido F. A., Edge A. C., 2018, ApJ, 857, 32
Bacon R. et al., 2010, in McLean I. S., Ramsay S. K., Takami H. eds, Proc. SPIE Conf. Ser. Vol. 7735, Ground-Based and Airborne Instrumentation for Astronomy III. SPIE, Bellingham, p. 773508
Bai Y., Zou H., Liu J., Wang S., 2015, ApJS, 220, 6
Baldwin J. A., Phillips M. M., Terlevich R., 1981, PASP, 93, 5
Bertin E., Arnouts S., 1996, A&AS, 117, 393
Bhattacharya S., Arnaboldi M., Hammer F., Yang Y., Gerhard O., Caldwell N., Freeman K. C., 2023, MNRAS, 522, 6010
Bhattacharya S., Arnaboldi M., Hartke J., Gerhard O., Comte V., McConnachie A., Caldwell N., 2019, A&A, 624, A132
Bittner A. et al., 2019, A&A, 628, A117
Blakeslee J. P. et al., 2010, ApJ, 724, 657
Bradley L. et al., 2023, astropy/photutils: 1.8.0, Zenodo, https://doi.org/10.5281/zenodo.7946442
Buzzoni A., 1989, ApJS, 71, 817
Buzzoni A., Arnaboldi M., Corradi R. L. M., 2006, MNRAS, 368, 877
Caon N., Capaccioli M., D'Onofrio M., 1994, A&AS, 106, 199
Capaccioli M., Held E. V., Nieto J.-L., 1987, AJ, 94, 1519
Cappellari M. et al., 2011, MNRAS, 413, 813
Cappellari M., 2017, MNRAS, 466, 798
Cappellari M., Copin Y., 2003, MNRAS, 342, 345
Cappellari M., Emsellem E., 2004, PASP, 116, 138
Cardelli J. A., Clayton G. C., Mathis J. S., 1989, ApJ, 345, 245
Cheng C. M. et al., 2024, MNRAS, 532, 3604
Ciardullo R., 2010, Publ. Astron. Soc. Aust., 27, 149
Ciardullo R., Durrell P. R., Laychak M. B., Herrmann K. A., Moody K., Jacoby G. H., Feldmeier J. J., 2004, ApJ, 614, 167
Ciardullo R., Feldmeier J. J., Jacoby G. H., Kuzio de Naray R., Laychak M. B., Durrell P. R., 2002, ApJ, 577, 31
Ciardullo R., Jacoby G. H., Ford H. C., Neill J. D., 1989, ApJ, 339, 53
Ciardullo R., Jacoby G. H., Harris W. E., 1991, ApJ, 383, 487
Ciardullo R., Sigurdsson S., Feldmeier J. J., Jacoby G. H., 2005, ApJ, 629, 499
Coccato L. et al., 2009, MNRAS, 394, 1249
Coccato L., Gerhard O., Arnaboldi M., 2010, MNRAS, 407, L26
Cortesi A. et al., 2013a, MNRAS, 432, 1010
Cortesi A. et al., 2013b, A&A, 549, A115
de Vaucouleurs G., de Vaucouleurs A., Corwin H. G., Jr, Buta R. J., Paturel G., Fouque P., 1991, Third Reference Catalogue of Bright Galaxies. Springer-Verlag, New York
Dopita M. A., Massaglia S., Bodo G., Arnaboldi M., Merluzzi P., 2000, in Kastner J. H., Soker N., Rappaport S., eds, ASP Conf. Ser. Vol. 199, Active Galaxies.Asymmetrical Planetary Nebulae II: From Origins to Microstructures. Astron. Soc. Pac., San Francisco, p. 423
Douglas N. G., Taylor K., 1999, MNRAS, 307, 190
Gerhard O. E., 1993, MNRAS, 265, 213
Gerhard O., Arnaboldi M., Freeman K. C., Kashikawa N., Okamura S., Yasuda N., 2005, ApJ, 621, L93
González-Martín O., Masegosa J., Márquez I., Guainazzi M., Jiménez-Bailón E., 2009, A&A, 506, 1107
Guérou A., Emsellem E., Krajnović D., McDermid R. M., Contini T., Weilbacher P. M., 2016, A&A, 591, A143
Harris C. R. et al., 2020, Nature, 585, 357
Hartke J. et al., 2018, A&A, 616, A123
Hartke J. et al., 2020, A&A, 642, A46
Hartke J. et al., 2022, A&A, 663, A12
Hartke J., Arnaboldi M., Longobardi A., Gerhard O., Freeman K. C., Okamura S., Nakata F., 2017, A&A, 603, A104
Henize K. G., Westerlund B. E., 1963, ApJ, 137, 747
Hernández-Martínez L., Peña M., 2009, A&A, 495, 447
Ho L. C., Li Z.-Y., Barth A. J., Seigar M. S., Peng C. Y., 2011, ApJS, 197, 21
Hunter J. D., 2007, Comput. Sci. Eng., 9, 90
Iodice E. et al., 2019, A&A, 627, A136
Jacoby G. H., 1989, ApJ, 339, 39
Jacoby G. H., Ciardullo R., Roth M. M., Arnaboldi M., Weilbacher P. M., 2024, ApJS, 271, 40
Jacoby G. H., De Marco O., 2002, AJ, 123, 269
Kartha S. S., Forbes D. A., Spitler L. R., Romanowsky A. J., Arnold J. A., Brodie J. P., 2014, MNRAS, 437, 273
Kormendy J., Fisher D. B., Cornell M. E., Bender R., 2009, ApJS, 182, 216
Kreckel K., Groves B., Bigiel F., Blanc G. A., Kruijssen J. M. D., Hughes A., Schruba A., Schinnerer E., 2017, ApJ, 834, 174
Kroupa P., 2001, MNRAS, 322, 231
Kuntschner H. et al., 2010, MNRAS, 408, 97
Lee M. G., Jang I. S., 2016, ApJ, 822, 70
Li Z.-Y., Ho L. C., Barth A. J., Peng C. Y., 2011, ApJS, 197, 22
Longobardi A., Arnaboldi M., Gerhard O., Coccato L., Okamura S., Freeman K. C., 2013, A&A, 558, A42
Longobardi A., Arnaboldi M., Gerhard O., Hanuschik R., 2015, A&A, 579, A135
Martin J., Xilouris K., Soker N., 2002, A&A, 391, 689
Martín-Navarro I. et al., 2021, A&A, 654, A59
McDermid R. M. et al., 2015, MNRAS, 448, 3484
McKinney W., 2010, in van der Walt S., Millman J. eds, Proceedings of the 9th Python in Science Conference. p. 51
Norris M. A., Sharples R. M., Kuntschner H., 2006, MNRAS, 367, 815
Pastorello N., Forbes D. A., Foster C., Brodie J. P., Usher C., Romanowsky A. J., Strader J., Arnold J. A., 2014, MNRAS, 442, 1003
Pedregosa F. et al., 2011, J. Mach. Learn. Res., 12, 2825
Pietrinferni A., Cassisi S., Salaris M., Castelli F., 2004, ApJ, 612, 168
Pietrinferni A., Cassisi S., Salaris M., Castelli F., 2006, ApJ, 642, 797
Pietrinferni A., Cassisi S., Salaris M., Hidalgo S., 2013, A&A, 558, A46
Pietrinferni A., Cassisi S., Salaris M., Percival S., Ferguson J. W., 2009, ApJ, 697, 275
Pulsoni C. et al., 2018, A&A, 618, A94
Pulsoni C., Gerhard O., Fall S. M., Arnaboldi M., Ennis A. I., Hartke J., Coccato L., Napolitano N. R., 2023, A&A, 674, A96
Renzini A., Buzzoni A., 1986, in Chiosi C., Renzini A. eds, Astrophysics and Space Science Library, Vol. 122, Spectral Evolution of Galaxies. Springer-Verlag, Berlin, p. 195
Richard J. et al., 2019, preprint (arXiv:1906.01657)
Rodriguez-Gomez V. et al., 2019, MNRAS, 483, 4140
Roth M. M. et al., 2018, A&A, 618, A3
Roth M. M., Jacoby G. H., Ciardullo R., Davis B. D., Chase O., Weilbacher P. M., 2021, ApJ, 916, 21
Sabbadin F., Minello S., Bianchini A., 1977, A&A, 60, 147
Sarzi M., Mamon G. A., Cappellari M., Emsellem E., Bacon R., Davies R. L., de Zeeuw P. T., 2011, MNRAS, 415, 2832
Schlegel D. J., Finkbeiner D. P., Davis M., 1998, ApJ, 500, 525
Sersic J. L., 1968, Atlas de Galaxias Australes. Observatorio Nacional Astronómico de Córdoba, Córdoba, Argentina
Shaver P. A., McGee R. X., Newton L. M., Danks A. C., Pottasch S. R., 1983, MNRAS, 204, 53
Soemitro A. A., Roth M. M., Weilbacher P. M., Ciardullo R., Jacoby G. H., Monreal-Ibero A., Castro N., Micheva G., 2023a, A&A, 671, A142
Soemitro A. A., Roth M. M., Weilbacher P. M., Ciardullo R., Jacoby G. H., Monreal-Ibero A., Castro N., Micheva G., 2023b, A&A, 671, A142
Spiniello C. et al., 2018, MNRAS, 477, 1880
Tonry J. L., Dressler A., Blakeslee J. P., Ajhar E. A., Fletcher A. B., Luppino G. A., Metzger M. R., Moore C. B., 2001, ApJ, 546, 681
Tully R. B. et al., 2013, AJ, 146, 86
Valenzuela L. M., Miller Bertolami M. M., Remus R.-S., Méndez R. H., 2025, A&A, 699, A371

van der Marel R. P., Franx M., 1993, ApJ, 407, 525
Vazdekis A., Sánchez-Blázquez P., Falcón-Barroso J., Cenarro A. J., Beasley M. A., Cardiel N., Gorgas J., Peletier R. F., 2010, MNRAS, 404, 1639
Villaver E., Stanghellini L., 2005, ApJ, 632, 854
Virtanen P. et al., 2020, Nat. Methods, 17, 261
Watkins A. E., Mihos J. C., Harding P., Feldmeier J. J., 2014, ApJ, 791, 38
Weilbacher P. M. et al., 2020, A&A, 641, A28
Zaritsky D., Gil de Paz A., Bouquin A. Y. K., 2015, MNRAS, 446, 2030
Zibetti S., Gallazzi A. R., Hirschmann M., Consolandi G., Falcón-Barroso J., van de Ven G., Lyubenova M., 2020, MNRAS, 491, 3562

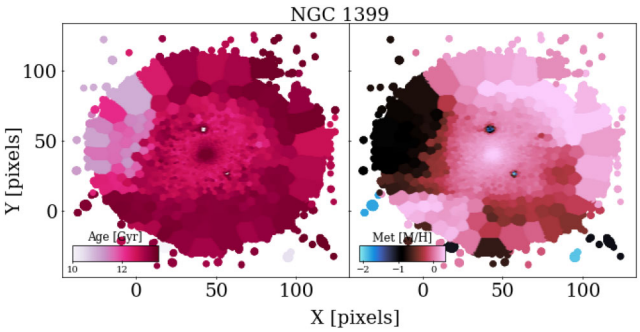

Figure A2. Stellar population properties of the stellar component of NGC 1399 as obtained with GIST.

APPENDIX A: STELLAR POPULATION PROPERTIES

In this appendix, we present our results from the analysis of the kinematics and properties of the stellar populations in each cube, following the methodology described in Section 3. For each galaxy, we present maps of the stellar kinematics parametrized by V, σ, h_3, and h_4 (e.g. Fig. A1) and the stellar ages and metallicities (e.g. Fig. A2. Light-weighted mean values were extracted from these maps, excluding the very central regions where we do not detect PNe (cf. Section 4.3), to use in the analysis presented in the discussion in Section 6.

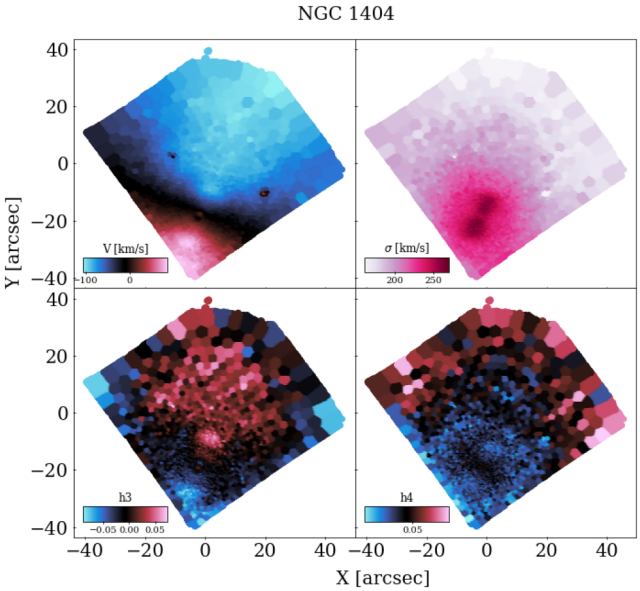

Figure A3. Kinematic properties of the stellar component of NGC 1404 as obtained with GIST.

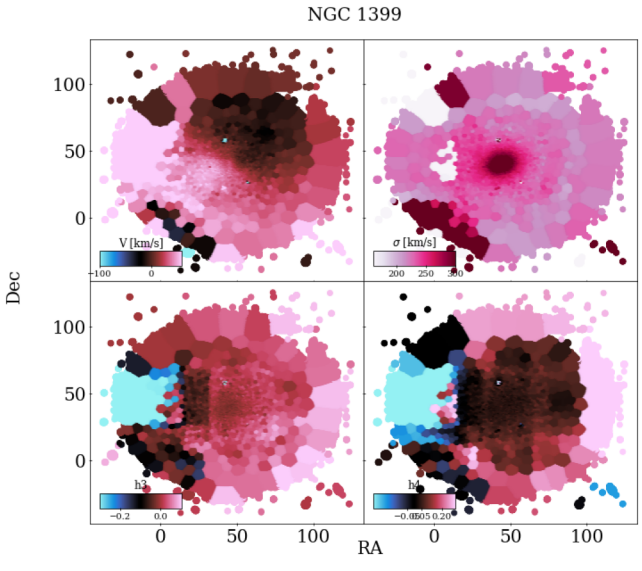

Figure A1. Kinematic properties of the stellar component of NGC 1399 as obtained with GIST.

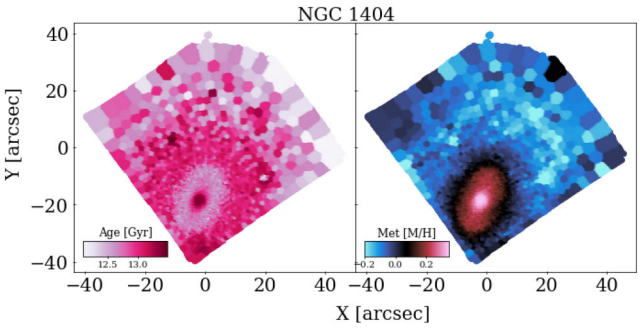

Figure A4. Stellar population properties of the stellar component of NGC 1404 as obtained with GIST.

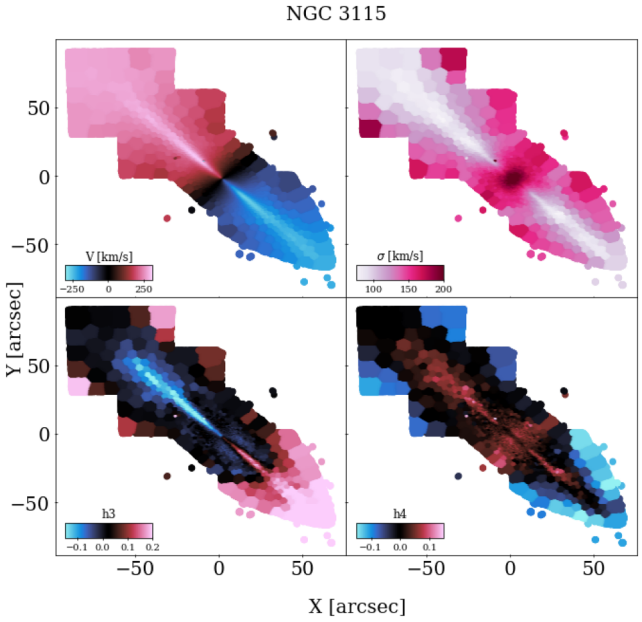

Figure A5. Kinematic properties of the stellar component of NGC 3115 as obtained with GIST.

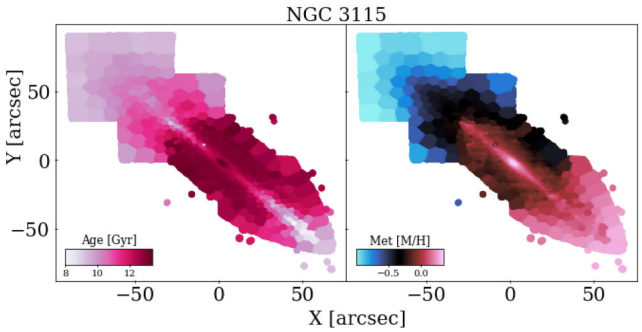

Figure A6. Stellar population properties of the stellar component of NGC 3115 as obtained with GIST.

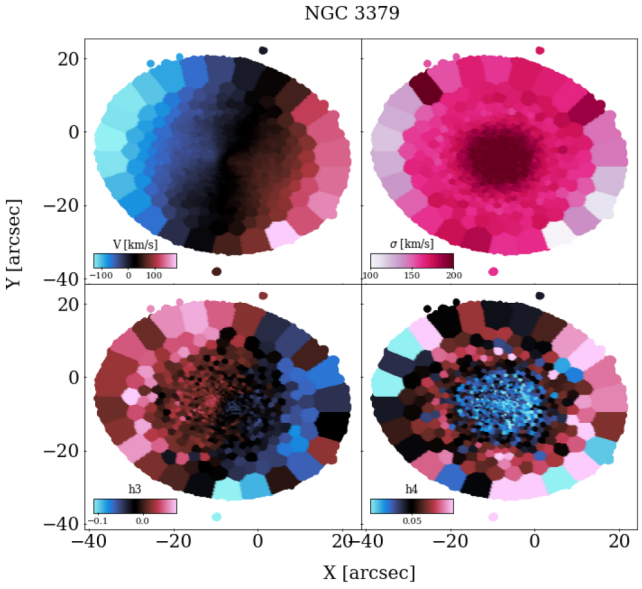

Figure A7. Kinematic properties of the stellar component of NGC 3379 as obtained with GIST.

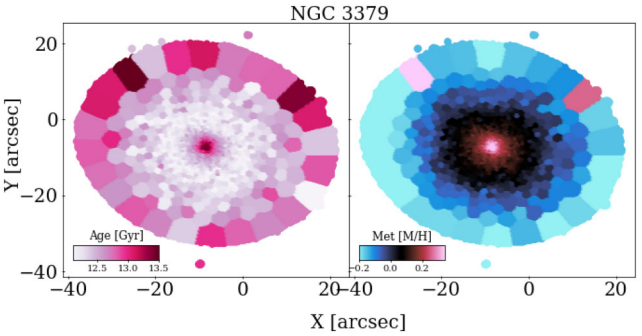

Figure A8. Stellar population properties of the stellar component of NGC 3379 as obtained with GIST.

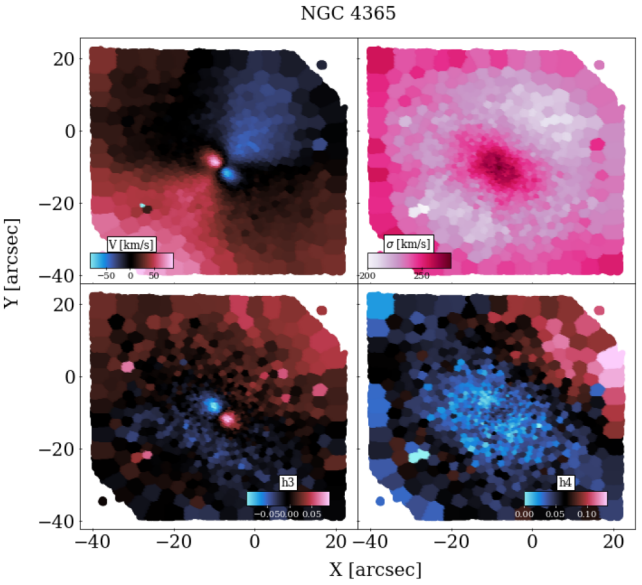

Figure A9. Kinematic properties of the stellar component of NGC 4365 as obtained with GIST.

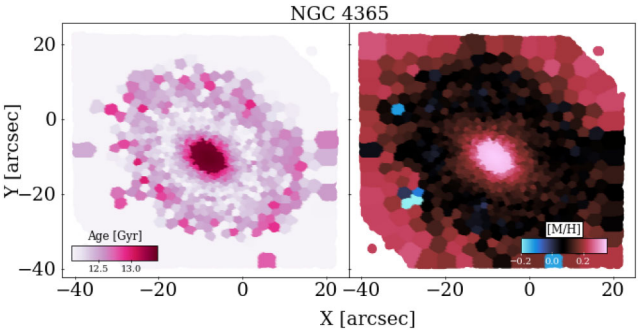

Figure A10. Stellar population properties of the stellar component of NGC 4365 as obtained with GIST.

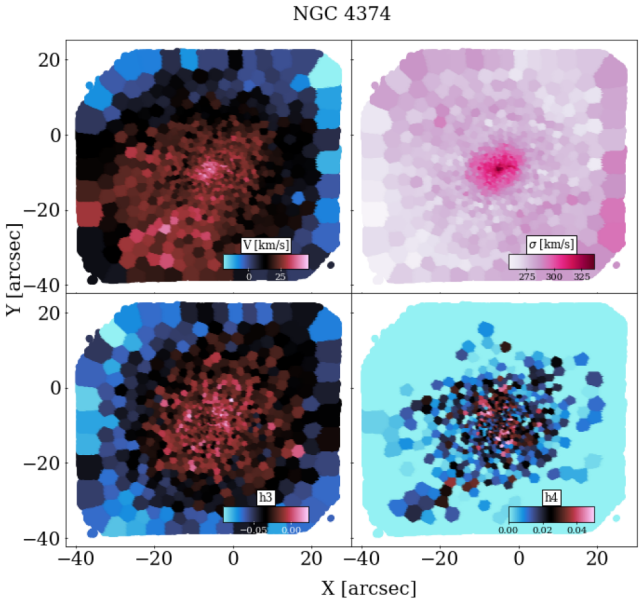

Figure A11. Kinematic properties of the stellar component of NGC 4374 as obtained with GIST.

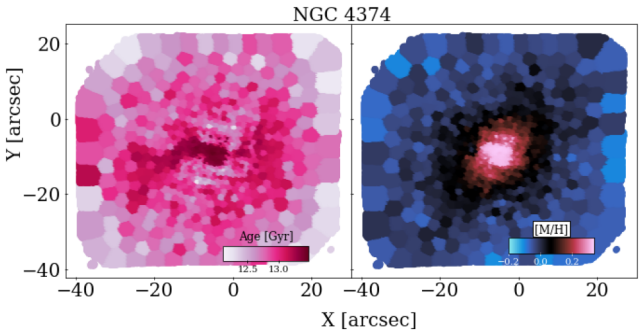

Figure A12. Stellar population properties of the stellar component of NGC 4374 as obtained with GIST.

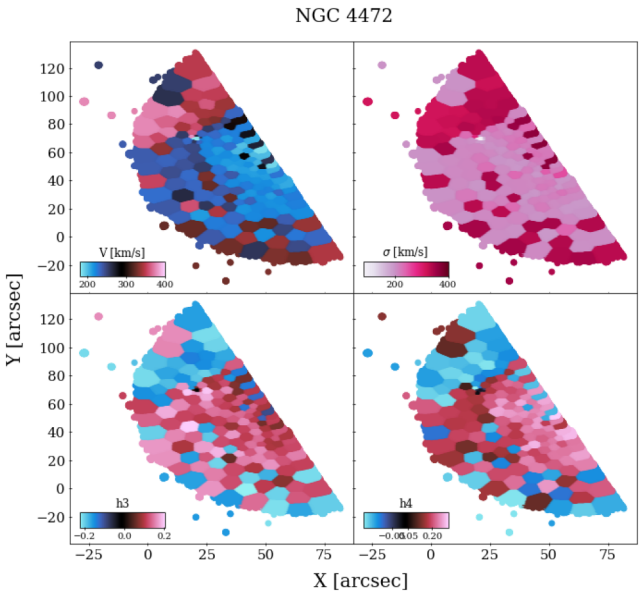

Figure A13. Kinematic properties of the stellar component of NGC 4472 as obtained with GIST.

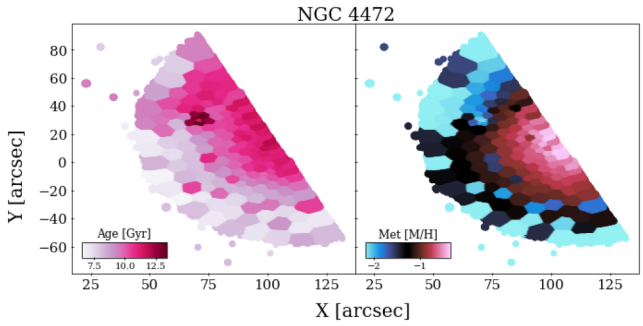

Figure A14. Stellar population properties of the stellar component of NGC 4472 as obtained with GIST.

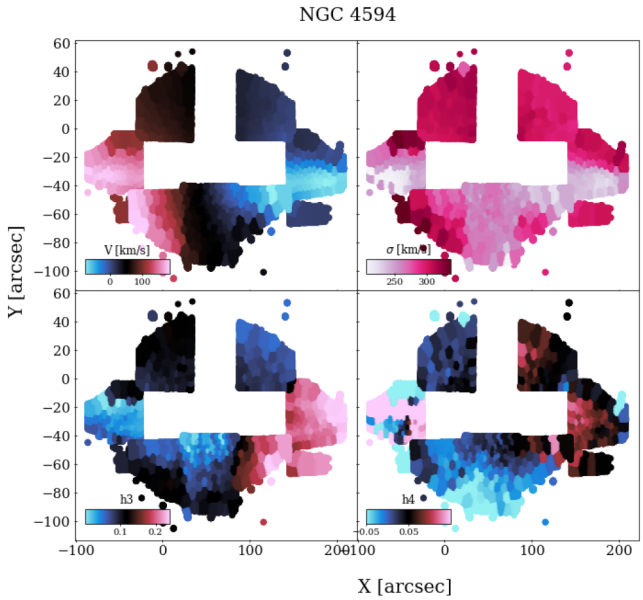

Figure A15. Kinematic properties of the stellar component of NGC 4594 as obtained with GIST.

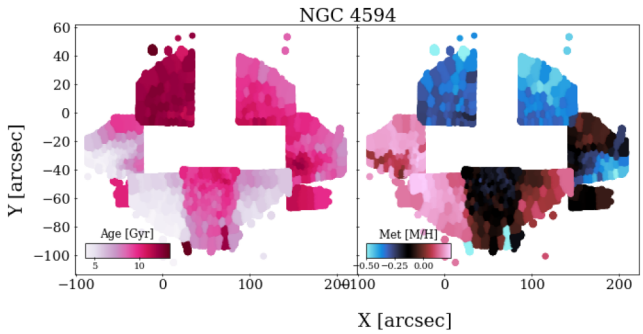

Figure A16. Stellar population properties of the stellar component of NGC 4594 as obtained with GIST.

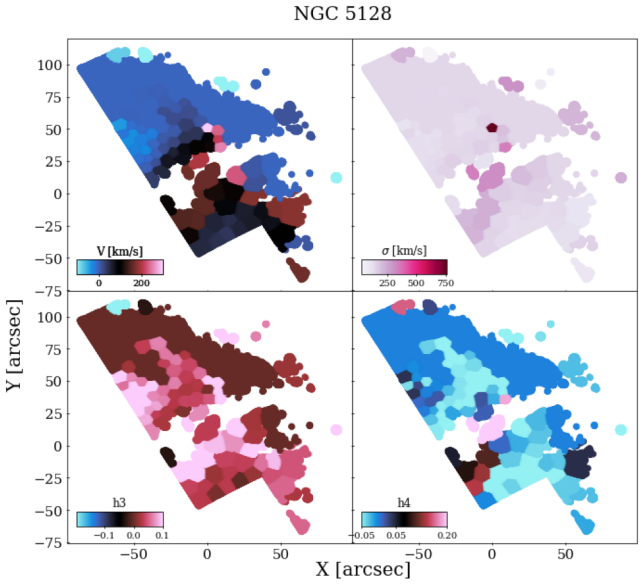

Figure A17. Kinematic properties of the stellar component of NGC 5128 as obtained with GIST.

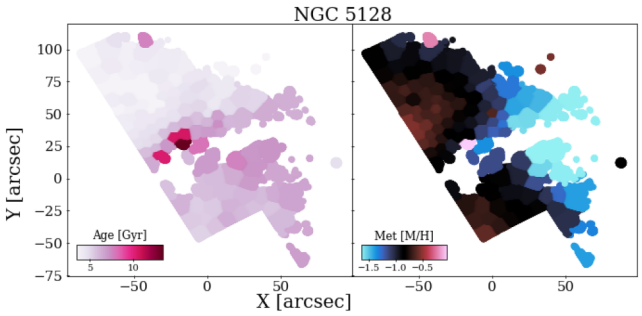

Figure A18. Stellar population properties of the stellar component of NGC 5128 as obtained with GIST.

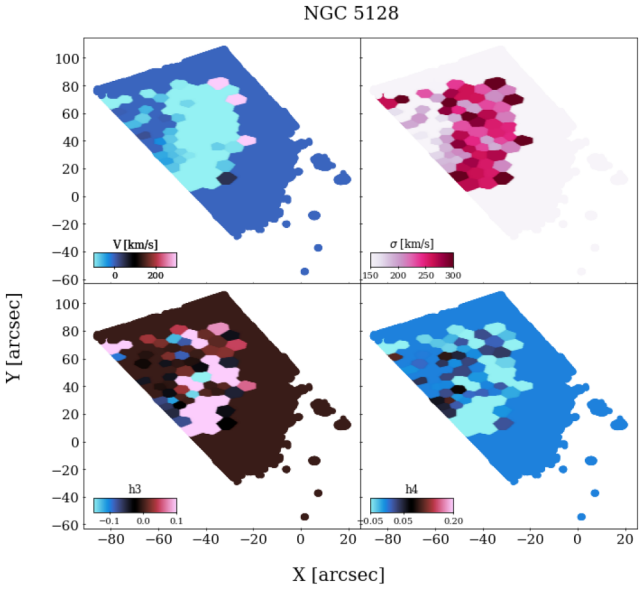

Figure A19. Kinematic properties of the stellar component of NGC 5128 as obtained with GIST.

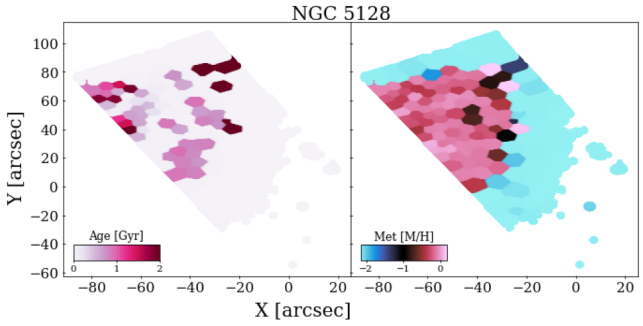

Figure A20. Stellar population properties of the stellar component of NGC 5128 as obtained with GIST.

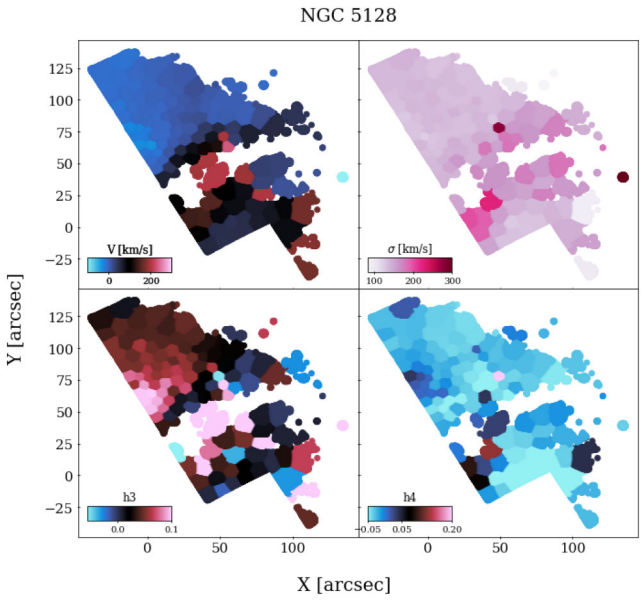

Figure A21. Kinematic properties of the stellar component of NGC 5128 as obtained with GIST.

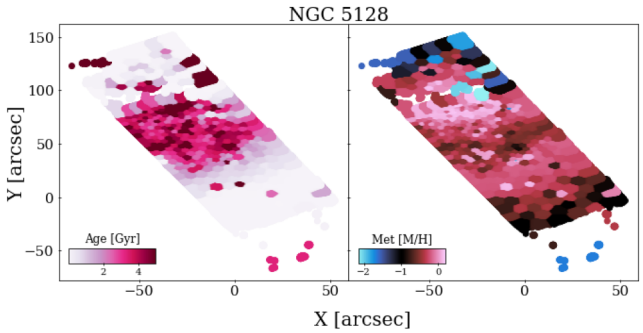

Figure A22. Stellar population properties of the stellar component of NGC 5128 as obtained with GIST.

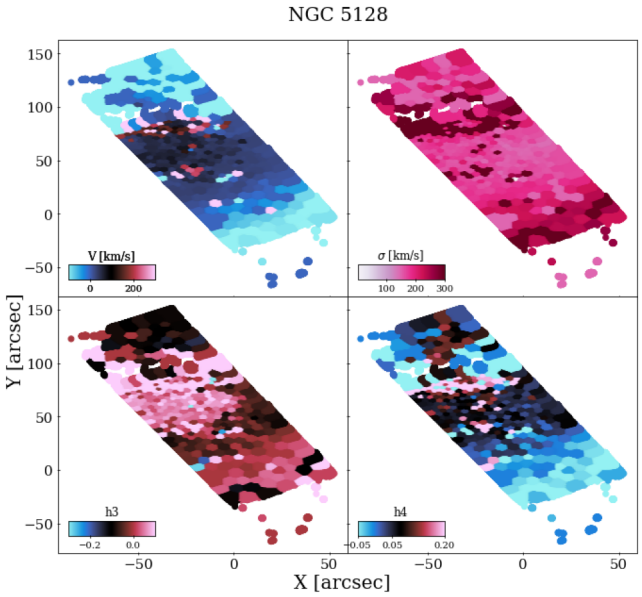

Figure A23. Kinematic properties of the stellar component of NGC 5128 as obtained with GIST.

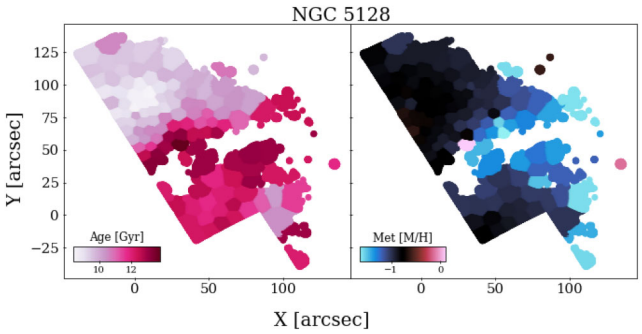

Figure A24. Stellar population properties of the stellar component of NGC 5128 as obtained with GIST.

APPENDIX B: PLANETARY NEBULAE ANALYSIS

In this appendix, we present the diagnostic diagrams for the sources detected in each galaxy, with blue points showing sources considered interlopers, and pink ones, PNe. The solid lines indicate the criteria described in Section 4.

We also present the PNLF for all galaxies. In all cases, a grey dashed histogram show the observed PNLF, and a histogram with pink solid lines indicates the PNLF corrected by completeness. The grey thick vertical bars indicate the errors. The analytic fits with a fixed and a variable bright cut-off are indicated with a dash–dotted light blue curve and a solid dark blue one, respectively.

Finally, we present the PN number density (pink crosses), offset to match the Sérsic fit to the surface brightness profile of each galaxy, shown with a solid black line.

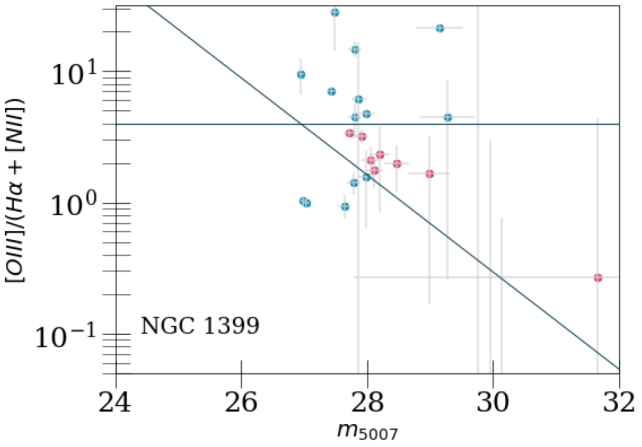

Figure B1. [O iii]/(Hα + [N ii]) line ratios as a function of [O III] apparent magnitude for the entire sample of objects detected in NGC 1399 using the [O III] field. Symbols and lines as described in Fig. 6.

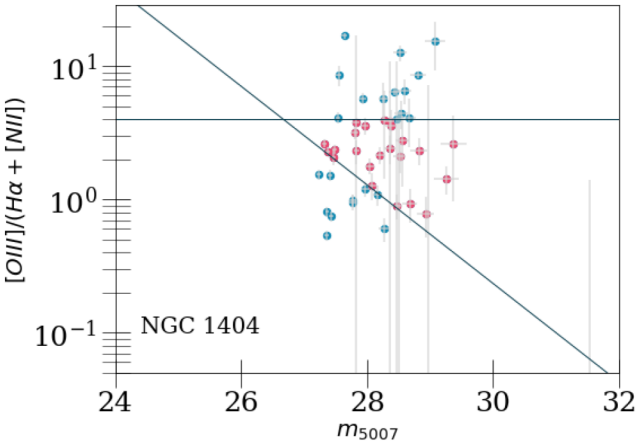

Figure B2. [O iii]/(Hα + [N ii]) line ratios as a function of [O III] apparent magnitude for the entire sample of objects detected in NGC 1404 using the [O III] field. Symbols and lines as described in Fig. 6.

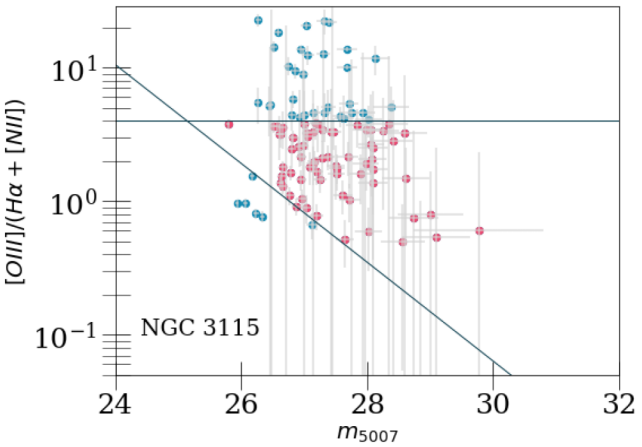

Figure B3. [O iii]/(Hα + [N ii]) line ratios as a function of [O III] apparent magnitude for the entire sample of objects detected in NGC 3115 using the [O III] field. Symbols and lines as described in Fig. 6.

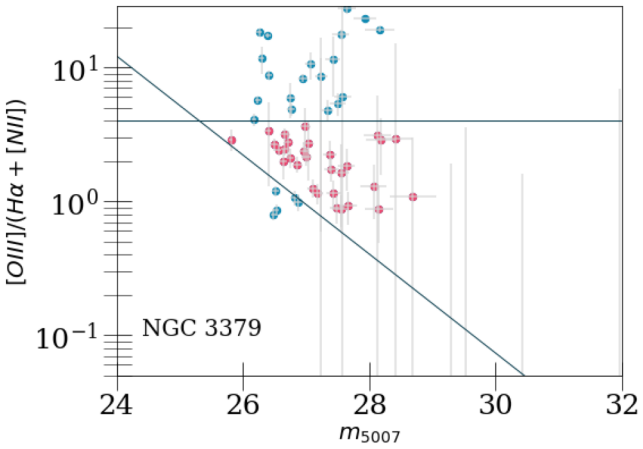

Figure B4. [O iii]/(Hα + [N ii]) line ratios as a function of [O iii] apparent magnitude for the entire sample of objects detected in NGC 3379 using the [O iii] field. Symbols and lines as described in Fig. 6.

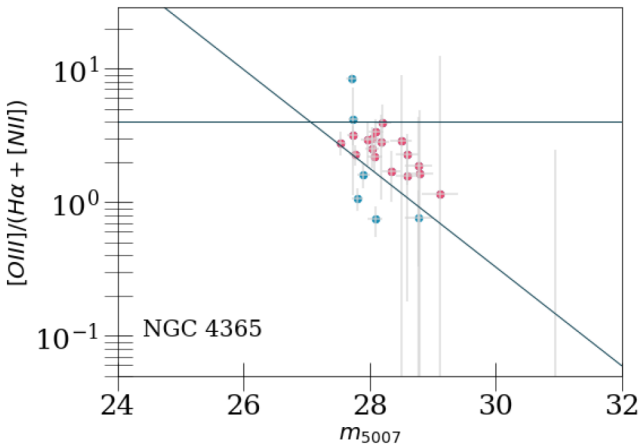

Figure B5. [O iii]/(Hα + [N ii]) line ratios as a function of [O iii] apparent magnitude for the entire sample of objects detected in NGC 4365 using the [O iii] field. Symbols and lines as described in Fig. 6.

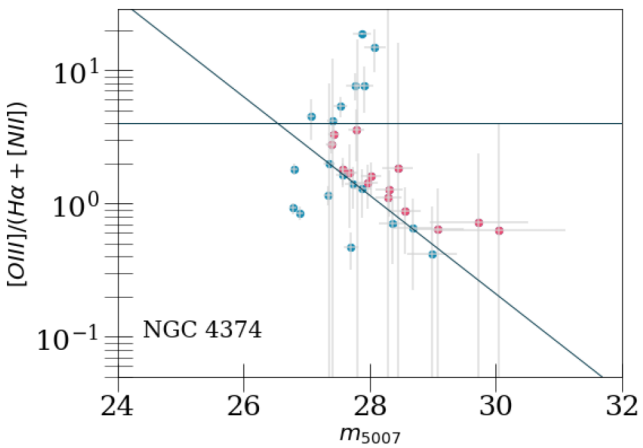

Figure B6. [O iii]/(Hα + [N ii]) line ratios as a function of [O iii] apparent magnitude for the entire sample of objects detected in NGC 4374 using the [O iii] field. Symbols and lines as described in Fig. 6.

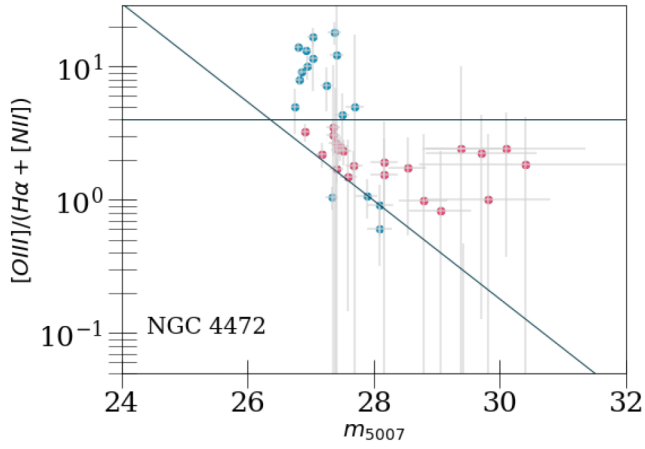

Figure B7. [O iii]/(Hα + [N ii]) line ratios as a function of [O iii] apparent magnitude for the entire sample of objects detected in NGC 4472 using the [O iii] field. Symbols and lines as described in Fig. 6.

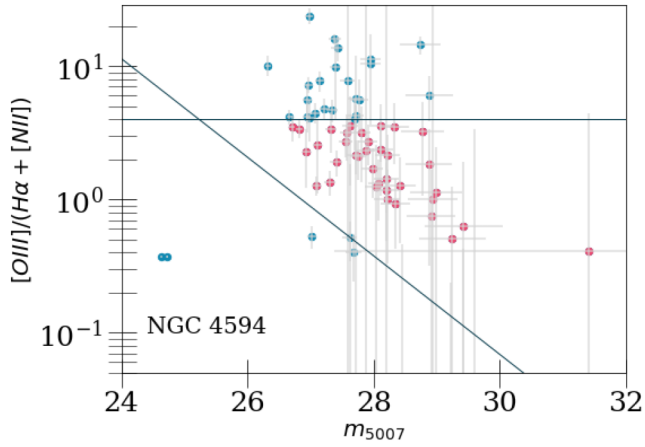

Figure B8. [O iii]/(Hα + [N ii]) line ratios as a function of [O iii] apparent magnitude for the entire sample of objects detected in NGC 4594 using the [O iii] field. Symbols and lines as described in Fig. 6.

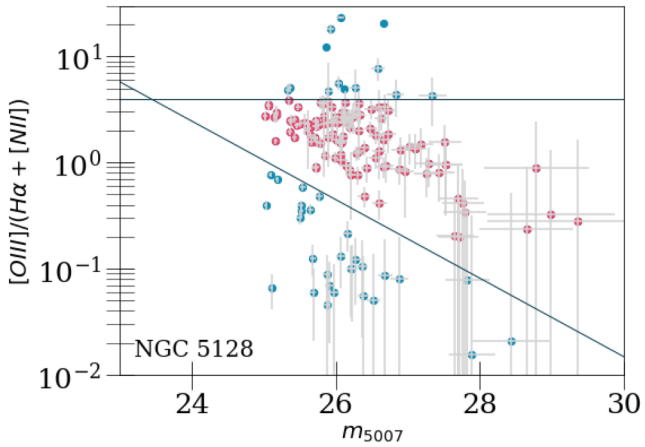

Figure B9. [O iii]/(Hα + [N ii]) line ratios as a function of [O iii] apparent magnitude for the entire sample of objects detected in NGC 5128 using the [O iii] field. Symbols and lines as described in Fig. 6.

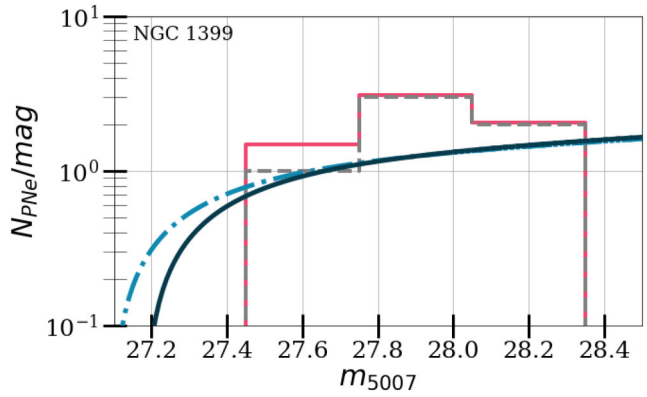

Figure B10. PNLF for PNe detected in NGC 1399, symbols and lines as described in Fig. 11.

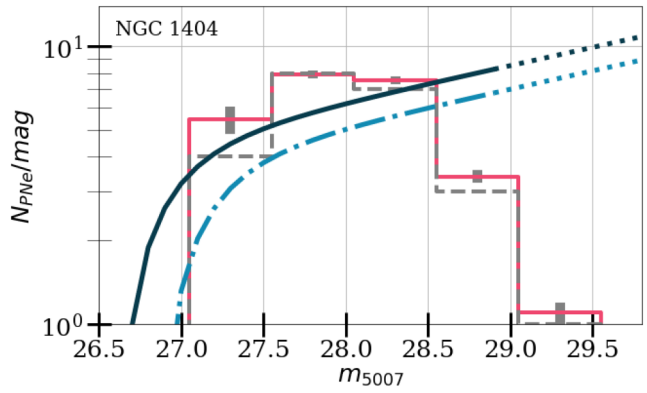

Figure B11. PNLF for PNe detected in NGC 1404, symbols and lines as described in Fig. 11.

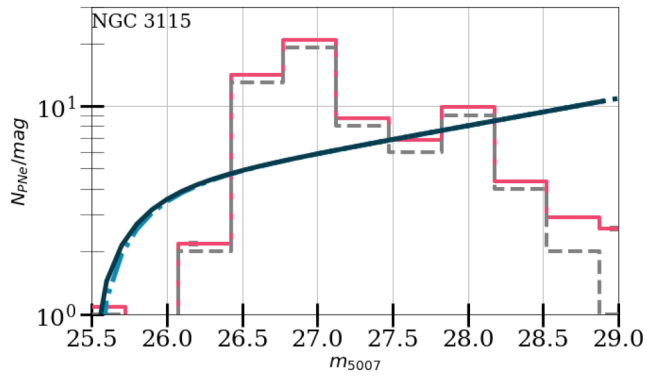

Figure B12. PNLF for PNe detected in NGC 3115, symbols and lines as described in Fig. 11.

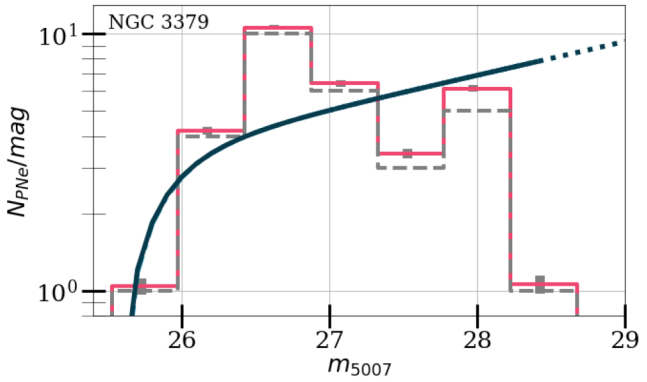

Figure B13. PNLF for PNe detected in NGC 3379, symbols and lines as described in Fig. 11.

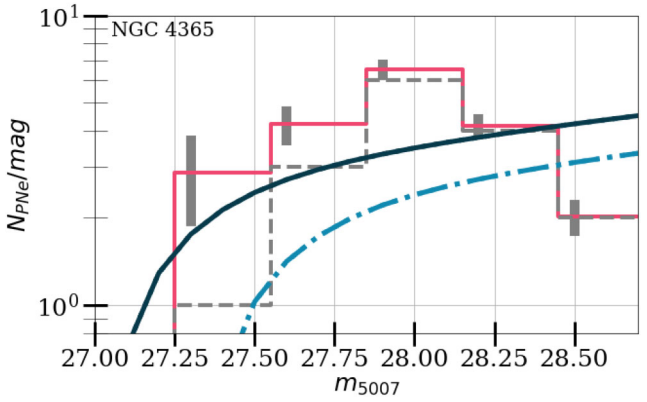

Figure B14. PNLF for PNe detected in NGC 4365, symbols and lines as described in Fig. 11.

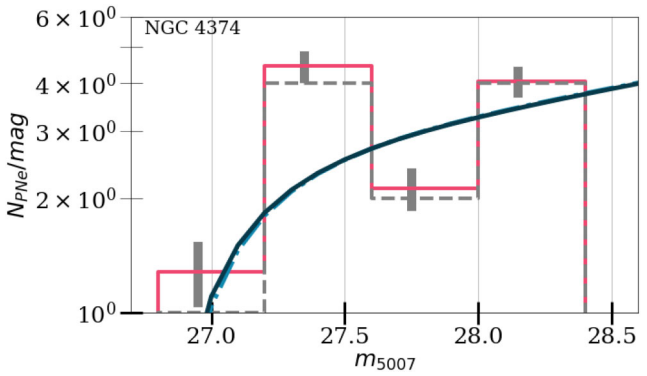

Figure B15. PNLF for PNe detected in NGC 4374, symbols and lines as described in Fig. 11.

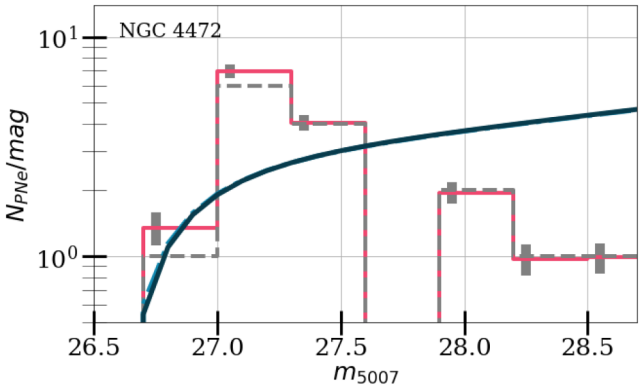

Figure B16. PNLF for PNe detected in NGC 4472, symbols and lines as described in Fig. 11.

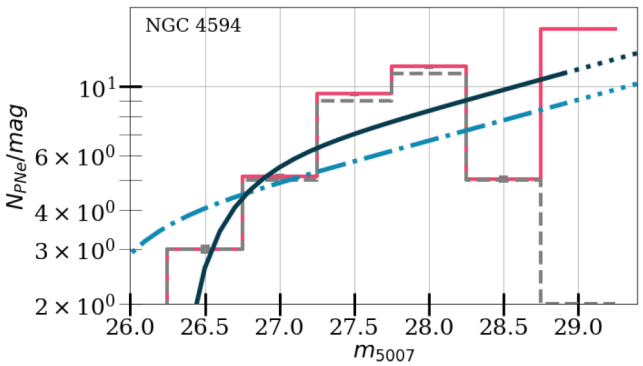

Figure B17. PNLF for PNe detected in NGC 4594, symbols and lines as described in Fig. 11.

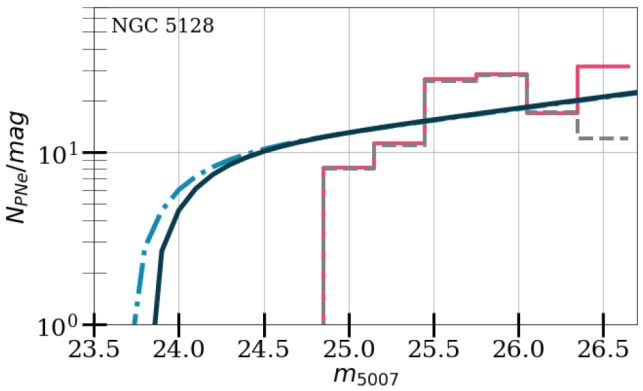

Figure B18. PNLF for PNe detected in NGC 5128, symbols and lines as described in Fig. 11.

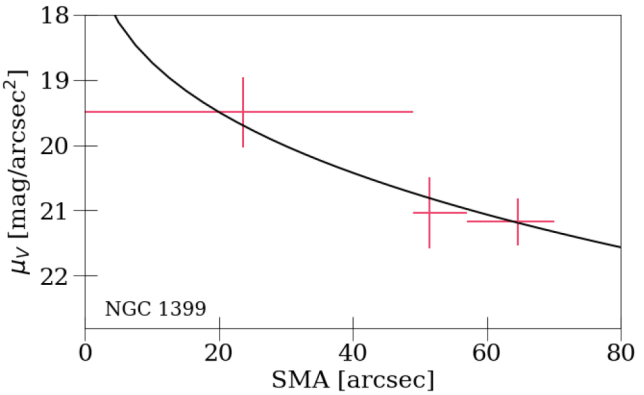

Figure B19. Sérsic fit to the surface brightness profile for NGC 1399 in the V-band shown in black solid line. The pink crosses indicate the PNe density offset by the fitted constant μ_0, with the errorbars signalling the size of the bin in the x-axis and the density error in the y-axis.

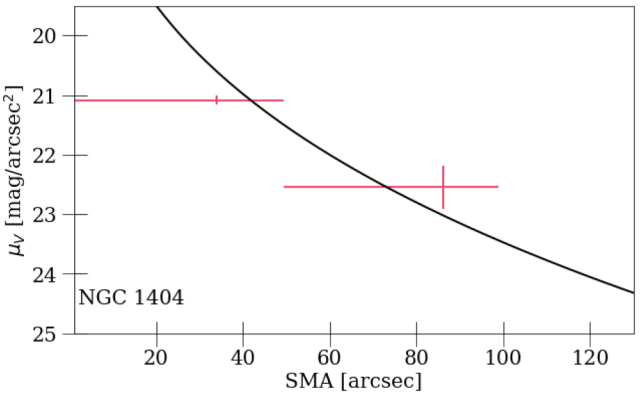

Figure B20. Sérsic fit to the surface brightness profile for NGC 1404 in the V-band shown in black solid line. The pink crosses indicate the PNe density offset by the fitted constant μ_0, with the errorbars signalling the size of the bin in the x-axis and the density error in the y-axis.

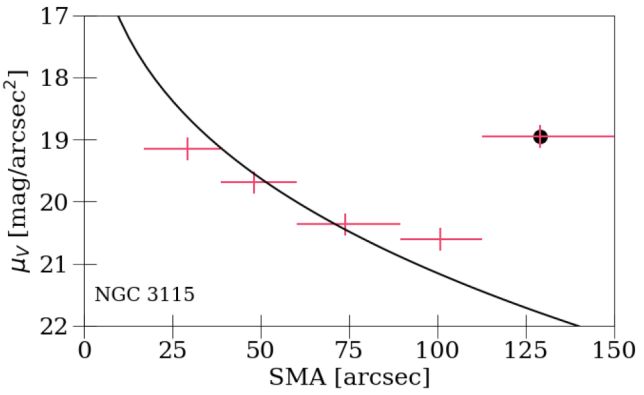

Figure B21. Sérsic fit to the surface brightness profile for NGC 3115 in the V-band shown in black solid line. The pink crosses indicate the PNe density offset by the fitted constant μ_0, with the errorbars signalling the size of the bin in the x-axis and the density error in the y-axis. The black dots indicate points excluded from the fit.

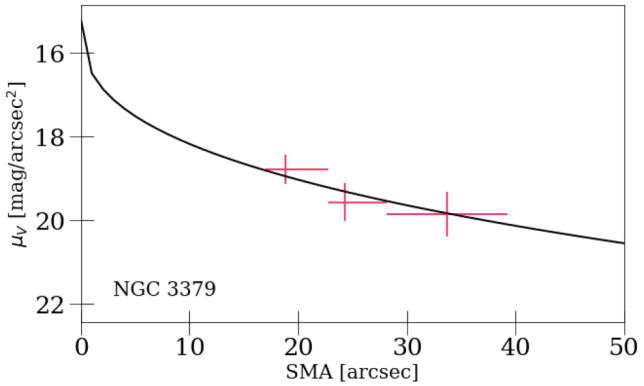

Figure B22. Sérsic fit to the surface brightness profile for NGC 3379 in the V-band shown in black solid line. The pink crosses indicate the PNe density offset by the fitted constant μ_0, with the errorbars signalling the size of the bin in the x-axis and the density error in the y-axis.

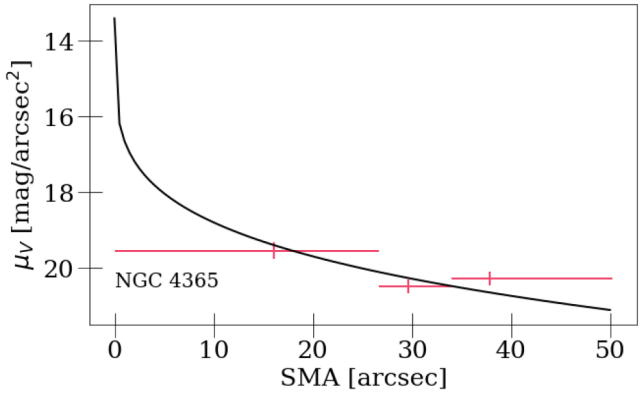

Figure B23. Sérsic fit to the surface brightness profile for NGC 4365 in the V-band shown in black solid line. The pink crosses indicate the PNe density offset by the fitted constant μ_0, with the errorbars signalling the size of the bin in the x-axis and the density error in the y-axis.

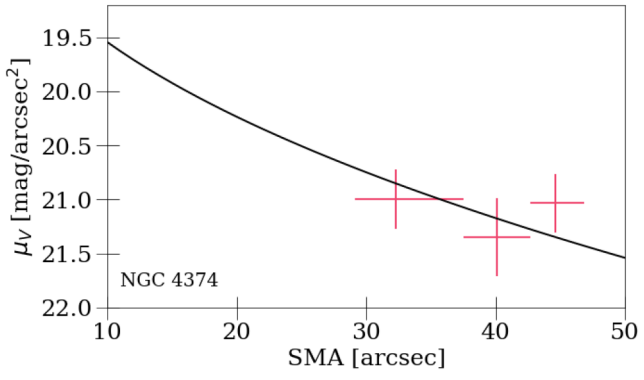

Figure B24. Sérsic fit to the surface brightness profile for NGC 4374 in the V-band shown in black solid line. The pink crosses indicate the PNe density offset by the fitted constant μ_0, with the errorbars signalling the size of the bin in the x-axis and the density error in the y-axis.

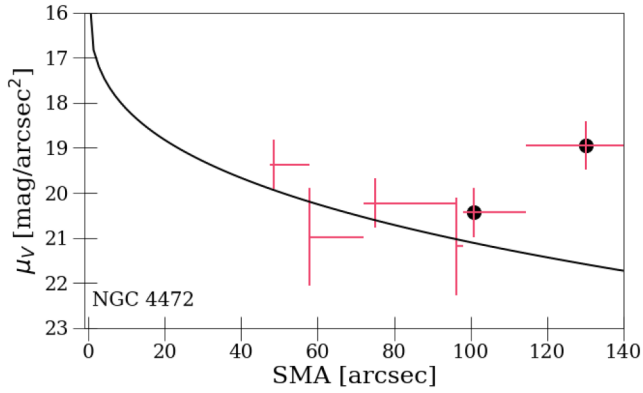

Figure B25. Sérsic fit to the surface brightness profile for NGC 4472 in the V-band shown in black solid line. The pink crosses indicate the PNe density offset by the fitted constant μ_0, with the errorbars signalling the size of the bin in the x-axis and the density error in the y-axis. The black dots indicate points excluded from the fit.

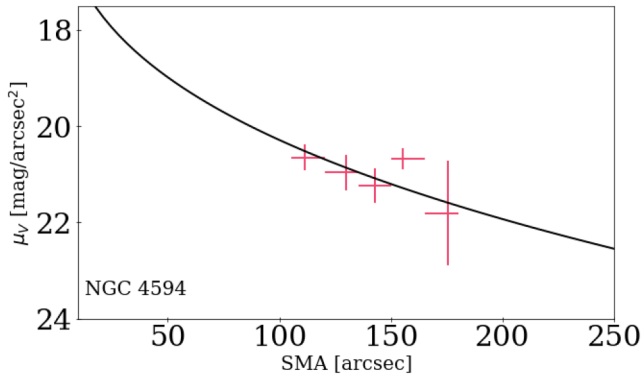

Figure B26. Sérsic fit to the surface brightness profile for NGC 4594 in the V-band shown in black solid line. The pink crosses indicate the PNe density offset by the fitted constant μ_0, with the errorbars signalling the size of the bin in the x-axis and the density error in the y-axis.

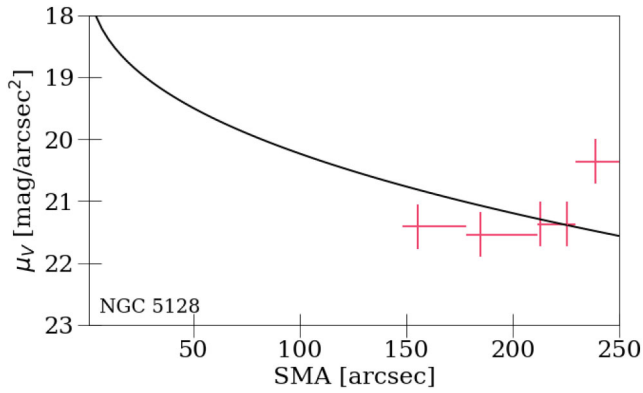

Figure B27. Sérsic fit to the surface brightness profile for NGC 5128 in the V-band shown in black solid line. The pink crosses indicate the PNe density offset by the fitted constant μ_0, with the errorbars signalling the size of the bin in the x-axis and the density error in the y-axis.

This paper has been typeset from a TEX/LATEX file prepared by the author.

© The Author(s) 2025.
Published by Oxford University Press on behalf of Royal Astronomical Society. This is an Open Access article distributed under the terms of the Creative Commons Attribution License (https://creativecommons.org/licenses/by/4.0/), which permits unrestricted reuse, distribution, and reproduction in any medium, provided the original work is properly cited.